TAMPEREEN TEKNILLINEN YLIOPISTO
TAMPERE UNIVERSITY OF TECHNOLOGY

Hannu Husu

# Electromagnetic Resonances and Local Fields in the Linear and Nonlinear Optical Response of Metal Nanostructures

Julkaisu 1008 • Publication 1008

Tampere 2011

Tampereen teknillinen yliopisto. Julkaisu 1008
Tampere University of Technology. Publication 1008

Hannu Husu

# Electromagnetic Resonances and Local Fields in the Linear and Nonlinear Optical Response of Metal Nanostructures

Thesis for the degree of Doctor of Science in Technology to be presented with due permission for public examination and criticism in Sähkötalo Building, Auditorium S1, at Tampere University of Technology, on the 2nd of December 2011, at 12 noon.

Tampereen teknillinen yliopisto - Tampere University of Technology
Tampere 2011

ISBN 978-952-15-2690-9 (printed)
ISBN 978-952-15-2762-3 (PDF)
ISSN 1459-2045

# ABSTRACT

The unique and tailorable properties of metal nanostructures show great prospects for future nanophotonics applications. However, the complicated interaction between the nanostructures and the electromagnetic field has many aspects still not known. Therefore, the basic research on the optical properties of metal nanostructures is essential for building a solid base for the future development towards real applications.

In this Work, T-shaped nanodimers and L-shaped nanoparticles, both made of gold, have been investigated. The goal has been to better understand the linear and nonlinear optical properties of the structures. The main focus has been in the plasmon resonances and the local electric fields, which depend on various parameters of the samples, and which are intimately connected.

In T-shaped nanodimers the local fields are very sensitive to the smallest structural details. Furthermore, the changes in the local-field distribution lead to variations in the second-order nonlinear response of the samples. In the linear response of L-shaped nanoparticles, we experimentally observed more higher-order resonances than anyone before. We also explained the origin of a short wavelength resonance, which had not been well understood earlier. In each case, the experimental observations were confirmed by numerical simulations.

Over the past years, the sample quality has improved significantly enabling fabrication of metal nanostructures with designable optical properties. Our first demonstrations of the new possibilities are related to resonance-domain structures. By utilizing the long-range diffractive coupling between the particles, we introduce a new concept for tailoring both the linear and nonlinear optical properties of arrays of metal nanostructures. The details in the mutual ordering of the particles can remarkably affect the diffractive coupling leading to unexpectedly large differences in the optical response of the samples.

# PREFACE

The research has been done in the Optics laboratory of the Department of Physics at Tampere University of Technology. Without the facilities provided by the University, the research would not have been possible. I acknowledge the Graduate School of the Tampere University of Technology for the financing of my research and the Academy of Finland for funding several research projects related to my research. I also acknowledge the Finnish Foundation for Technology Promotion for a personal grant.

I acknowledge my supervisor professor Martti Kauranen for all the guidance and constructive discussions during the research work towards the Thesis. I also acknowledge Brian Canfield for all the help, when starting the research on the topic.

As our laboratory does not have any equipment for fabricating the samples, the collaborators are essentially important. All the samples investigated in this Thesis have been fabricated at the University of Eastern Finland. Thus, I acknowledge Janne Laukkanen and Joonas Lehtolahti, who fabricated the samples for us, and professors Markku Kuittinen and Jari Turunen, for supervising the fabrication. I have also investigated and published results on structures fabricated at the Optoelectronics Research Center of the Tampere University of Technology. Although those results are not included in the Thesis, I still would like to thank Juha Kontio, who has made billions of tiny nanocones for us.

During the years I have been working in the Optics laboratory, the atmosphere has been simply great. First of all, I would like to thank Tapsa, Miro and Jaakko for nice company and interesting discussions during the lunch breaks in the coffee room. Secondly, I would like to address special thanks to my current and past roommates; Piotr, Fuxiang, Timo and Pauliina. Of all the other colleagues, I would like to mention: Francisco, Goëry, Henna, Iita, Jouni, Juha, Kalle, Mariusz, Matti, Mikael, Mikko, Robert, Roope, Sami, Samuli, Stefano, Tuomas, and our secretaries Inkeri and Hanna.

There is one more special group, which deserves mentioning. As sports, in general, is an important part of my life, the weekly floorball session has been always a real joy and a place to lose all the remaining energy. Thanks to all, who have been attending the floorball sessions.

Last, but definitely not least, I would like to thank my wife Johanna and my son Aleksi. You have shown me that there are even more important things than research.

# TABLE OF CONTENTS

# LIST OF FIGURES

# LIST OF TABLES

# SYMBOLS AND ABBREVIATIONS

| | |
|---|---|
| $a$ | Array period |
| $A_{jk}$ | Macroscopic response tensor components |
| $A_{jkl}$ | Nonlinear response tensor components |
| $c$ | Speed of light |
| $D$ | Complex denominator function |
| $E$ | Electric field, scalar |
| $E_0$ | Electric field amplitude |
| $\boldsymbol{E}$ | Electric field, vector |
| $G$ | Length of the grating vector |
| $i$ | Imaginary unit |
| $I$ | Intensity |
| $\boldsymbol{k}$ | Wave vector |
| $k_0$ | Propagation constant in vacuum |
| $k_{mode}$ | Propagation constant of surface mode |
| $k_{SP}$ | Propagation constant of surface plasmon |
| $k_t^{inc}$ | Tangential component of the incident wave vector |
| $L$ | Surface plasmon propagation length |
| $n$ | Index of refraction |
| $n_{Re}$ | Real part of index of refraction |
| $n_{Im}$ | Imaginary part of index of refraction |
| $N_p$ | Number of particles in a unit cell |
| $\boldsymbol{P}$ | Material polarization, vector |
| $r$ | Particle radius |
| | |
| $\alpha$ | Polarizability |
| $\alpha_{abs}$ | Absorption coefficient |
| $\gamma$ | Damping constant |
| $\gamma_D$ | Damping rate in the Drude model |
| $\delta$ | Skin depth |
| $\Delta$ | Full-width half-maximum |
| $\epsilon$ | Dielectric function, relative permittivity |
| $\lambda$ | Wavelength |
| $\mu$ | Permeability |
| $\chi^{(1)}$ | Linear susceptibility |
| $\chi^{(n)}$ | *n*th-order nonlinear susceptibility |

| | |
|---|---|
| $\omega$ | Angular frequency |
| $\omega_0$ | Resonance frequency |
| $\omega_p$ | Plasma frequency |

| | |
|---|---|
| CDR | Circular-difference response |
| EBL | Electron-beam lithography |
| FDTD | Finite-difference time-domain |
| FMM | Fourier modal method |
| FOM | Figure of merit |
| FWHM | Full-width half-maximum |
| LCP | Left-circular polarization |
| NRT | Nonlinear response tensor |
| RCP | Right-circular polarization |
| SEM | Scanning-electron microscope |
| SERS | Surface enhanced Raman scattering/spectroscopy |
| SH | Second-harmonic |
| SHG | Second-harmonic generation |
| SP | Surface plasmon |

# THESIS PUBLICATIONS

**Publication 1**

Brian K. Canfield, Hannu Husu, Janne Laukkanen, Benfeng Bai, Markku Kuittinen, Jari Turunen, and Martti Kauranen. *Local Field Asymmetry Drives Second-Harmonic Generation in Noncentrosymmetric Nanodimers.* Nano Letters **7**, 1251 (2007).

**Publication 2**

Hannu Husu, Brian K. Canfield, Janne Laukkanen, Benfeng Bai, Markku Kuittinen, Jari Turunen, and Martti Kauranen. *Chiral Coupling in Gold Nanodimers.* Applied Physics Letters **93**, 183115 (2008). Selected for the Virtual Journal of Nanoscale Science & Technology 18, issue 20, November 17, 2008.

**Publication 3**

Hannu Husu, Jouni Mäkitalo, Janne Laukkanen, Markku Kuittinen, and Martti Kauranen. *Particle plasmon resonances in L-shaped gold nanoparticles.* Optics Express **18**, 16601 (2010).

**Publication 4**

Hannu Husu, Jouni Mäkitalo, Roope Siikanen, Goëry Genty, Henna Pietarinen, Joonas Lehtolahti, Janne Laukkanen, Markku Kuittinen, and Martti Kauranen. *Spectral control in anisotropic resonance-domain metamaterials.* Optics Letters **36**, 2375 (2011).

**Publication 5**

Hannu Husu, Roope Siikanen, Joonas Lehtolahti, Janne Laukkanen, Markku Kuittinen, and Martti Kauranen. *Metamaterials with tailored nonlinear optical response.* Submitted to Nano Letters.

## SHORT SUMMARIES OF THE PUBLICATIONS

**Publication 1**

We investigated second-harmonic generation from T-shaped gold nanodimers, where the horizontal and vertical bars of the dimer structure were separated by a gap. The gap dependence of the second-harmonic signal was completely unexpected, but the results were explained by considering the symmetry of the local electric field distribution. The main result was that even small changes in the sample geometry can significantly affect the local fields, which furthermore affects the second-harmonic generation efficiency.

**Publication 2**

We investigated the same set of T-nanodimers as in Publication 1. We found that the vertical bar of the structure was slightly tilted with respect to the horizontal bar, which led to chiral symmetry breaking and different efficiency of second-harmonic generation for the two circular polarizations of fundamental light. The results were explained by considering the local field distributions for the two circular polarization states. The distribution depended not only on the tilt of the vertical bar, but also on the gap size.

**Publication 3**

We investigated the linear properties of L-shaped gold nanoparticles. We experimentally observed four higher-order resonances, which is more than anyone else has observed for samples with similar dimensions. We also explained the short wavelength resonances to be plasmon resonances related to the width of the structure, although earlier they had been misinterpreted as volume plasmons. All the observations were confirmed by the local electric field calculations.

**Publication 4**

We investigated the linear properties of resonance-domain structures consisting of L-shaped nanoparticles, where the mutual orientation between the particles was varied. The changes in the mutual orientation double the period of the structure in one or two directions, which opens diffraction orders designed to occur at the plasmonic resonances of the particles. The diffractive coupling between the particles affects the spectra significantly leading to very narrow or very broad resonances depending on the details of the particle ordering.

**Publication 5**

We demonstrated new possibilities for tailoring the second-order nonlinear response of arrays of L-shaped metal nanoparticles by controlling the mutual order-

ing of the particles. We showed that the results differed from the orientational average of the responses of the individual particles. Furthermore, we compared two samples with a minor difference in the sample layout, but a huge difference in the second-harmonic response. The results were explained in terms of the spectral differences discussed in Publication 4.

## AUTHOR'S CONTRIBUTION

The results obtained and reported in the publications have contributions from a group of people. The contribution of the Author of this Thesis is estimated in the table below. The table is divided into three parts. Preparation includes designing the samples and all the required background work before that. Experiments include deciding the experiment type, building the measurement setup and performing the measurements. It also involves supervising younger students in the measurements. Reporting includes analyzing the measurement data and reporting the results in a publication.

| | Preparation | Experiments | Reporting |
|---|---|---|---|
| **Publication 1** | 50 % | 80 % | 20 % |
| **Publication 2** | 60 % | 90 % | 80 % |
| **Publication 3** | 80 % | 70 % | 90 % |
| **Publication 4** | 80 % | 60 % | 90 % |
| **Publication 5** | 80 % | 60 % | 90 % |

# 1.

# INTRODUCTION

Metal nanoparticles have a long historical background in staining of glass windows and ceramics[1]. The optical response of such materials was first explained by Gustav Mie in 1908[2], and it is now understood that such intense colors arise from the plasmon resonances of small metal particles embedded in the material. Nowadays, research on metal nanoparticles and nanostructures is an extremely active research topic, and the research field investigating the interaction between light and nanoparticles is called *nanoplasmonics*.

## 1.1. METAL NANOSTRUCTURES

The optical properties of metal nanoparticles are based on plasmon resonances, which are collective oscillations of the conduction electrons in the particles. The resonances can greatly enhance the local electromagnetic fields, which is the basis of most of their applications. The plasmon resonances depend on particle dimensions, material, surrounding material and the arrangement of the particles, and thus, the properties can be tailored to match the requirements of different purposes. Furthermore, metal nanostructures can be designed to have special optical properties not even found in the naturally occurring materials. The unique properties and easy tailorability thus enables metal nanostructures to be used in the future nanophotonics applications.

The theory of Mie explains the interaction between small spherical particles and electromagnetic field of light[2]. The response of spherical particles and ellipsoids can be calculated analytically[3]. However, for more complicated structures, there is no analytical theory describing their optical properties. Thus, during the past decades many different types of particles and arrangements have been investigated both experimentally and by numerical simulations in order to understand what types of structures can produce different desirable functions.

The research in the past 10-20 years has covered different types of structures, of which the simplest are spherical, ellipsoidal and rod-like particles[3,4]. More complex structures include, for example, nanotriangles[5], nanorings[6], nanoshells[7,8] and U-shaped split-ring resonators[9,10]. In addition to single particle structures, coupled structures with several particles have also been investigated[11-13]. The basic understanding has thus been significantly increasing with the structural complexity adding new degrees of freedom for optimizing the responses.

The applications for metal nanostructures are numerous. Weak optical processes, like Raman scattering[14,15] and second-harmonic generation[16,17], can be significantly enhanced by strong local electromagnetic fields in metal nanostructures. In addition, the optical properties of nanostructures are very sensitive to the dielectric properties of the surrounding material, which forms the basis for plasmon sensors[18,19].

The properties of the electric field and propagation of the fields can also be controlled in the nanoscale. Plasmonic structures can be used for nanoscale focusing[20,21], plasmonic polarizers[22], miniature wave plates[23] and optical filters[24]. The emission pattern can be controlled by nanoantennas[25,26] and plasmonic waveguides can control the propagation of the fields in the structures[27]. Metamaterials with negative index of refraction can be used to focus light beyond the diffraction limit enabling high resolution imaging and lithography[28,29].

So far the research on metal nanostructures has focused mainly on their linear properties, but the possibility of local-field enhancement makes the structures particularly interesting also for nonlinear optics. It is evident that the nonlinear properties will attract more attention in the near future. This Thesis presents one of the first systematic studies, where the linear and nonlinear optical properties of metal nanostructures are simultaneously studied and correlated.

## 1.2. THIS WORK

In our laboratory, the research on metal nanoparticles began already in 2001 and the first article was published by Tuovinen et al. in 2002[30]. Our laboratory was thus among the first ones to start systematic studies of the nonlinear properties of metal nanostructures. The investigated particle shape was chosen to be L, because it is noncentrosymmetric, as required for second-harmonic generation, but it is also a simple shape with one mirror plane. Since then a lot of research has been done on investigating the linear and nonlinear properties of L-shaped metal nanoparticles. The research has addressed the resonance wavelength dependence on the particle dimensions, the symmetry breaking in the optical response of the particles[31], the chiral symmetry breaking induced by the defects in the parti-

cles[32], the effect of the defects in the second-harmonic generation from the particles[33], and also the effect of higher multipoles, which are associated with the defects[34].

In this Work, the linear and nonlinear optical properties of T-shaped gold nanodimers and L-shaped gold nanoparticles have been investigated. The T shape was also chosen due to its noncentrosymmetry, as required for second-harmonic response. In addition, both T and L shapes have fairly simple geometry and symmetry, which simplifies the analysis of the results. It is important to note that, in contrary to the common approach, the structures investigated in this Work have been designed from the point of view of nonlinear optics.

The main focus has been in the electromagnetic resonances and the local electric fields in the structures. The resonances have been investigated by measuring the linear spectra of the structures, which were also confirmed by numerical simulations. The local fields in the structures have also been simulated numerically. The nonlinear response has been investigated using polarization-dependent measurements to address the effective tensorial properties of the samples.

The main observation is that both the linear and nonlinear properties of metal nanostructures depend on the smallest details of the samples. By carefully controlling the details, one can tailor the response of the structures in unprecedented ways opening completely new concepts in the design and optimization of metal nanostructures for future nanophotonics applications.

## 1.3. Structure of the Thesis

The introductory part of the Thesis describes all the background information needed to understand the results obtained in the five publications at the end of the Thesis. In Chapter 2, the relevant background theory is explained. It introduces the electromagnetic properties of metals, which give rise to the plasmon resonances. Chapter 2 also covers the basics of second-harmonic generation and the theory behind diffractive coupling effects.

Chapter 3 gives a review of the research on metal nanostructures. It covers the different types of structures investigated and some of the most important results are discussed. The chapter includes also descriptions of the most interesting applications of metal nanostructures. Chapter 4 describes the samples and their fabrication. It also covers the experimental setups used in the optical measurements and the relevant theory used for analyzing the measurement results.

Chapter 5 covers the basic results, which are essential for understanding the publications. Chapter 5 also summarizes the main results from the Thesis publications. Finally, Chapter 6 concludes the Thesis and opens ideas for future research.

# 2.

# THEORETICAL BACKGROUND

This Chapter covers the background theory in order to build a base for the following chapters. The Chapter includes the basics of optics in metals, especially plasmons, which determine the optical properties of metal nanoparticles. The Chapter also covers the nonlinear response and how it is connected to the measurements. Finally, the Chapter describes the fundamentals of diffractive coupling between nanoparticles.

## 2.1. ELECTROMAGNETICS OF METALS

In general, the interaction between any material and the electromagnetic field can be described by the Maxwell's equations and the constitutive relations[35]. The same approach is valid also for metals. In this Work we have investigated the optical properties of metal nanostructures. Thus, it is important to note that the classical approach using Maxwell's equations is completely valid also for small particles down to a few nanometers[36].

### Dielectric function

The dielectric properties of a medium are described by the relative permittivity $\epsilon$ of the material, also known as the dielectric function. For dielectric materials, the permittivity is almost constant over a broad spectral range and also real-valued. For metals, the dielectric function is more complicated, as shown in Figure 2.1 for gold. Due to their conductivity, metals have a strong imaginary part of $\epsilon$ and, even more importantly, the real part is negative and can be very large. The negative real part of $\epsilon$ is essential for obtaining the plasmonic resonances in metal nanoparticles.

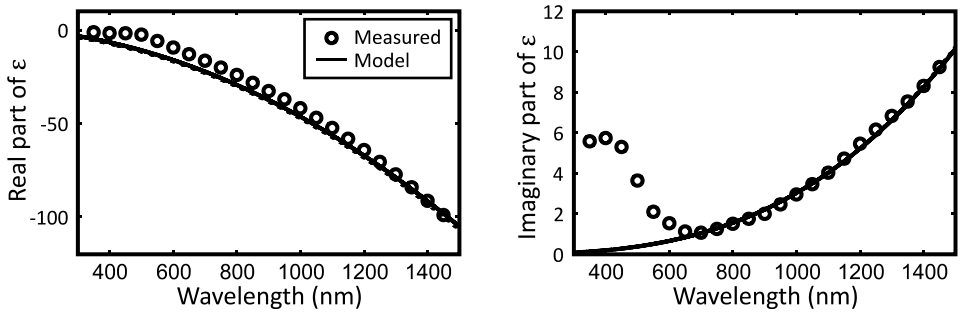


**Figure 2.1** Measured dielectric constant values (circles) for gold from *Johnson and Christy*[37] and a Drude model (Equation (2.1)) fitted to the values (line). Dashed line, which almost completely overlaps with the solid line, corresponds to the approximate model of Equation (2.6).

The metal response to the applied electric field can be described using a plasma model, where a cloud of free electrons is considered to move against a background of positive cores. By solving a simple equation of motion for the electrons, the Drude model for the dielectric function is obtained[36]

$$\epsilon(\omega) = 1 - \frac{\omega_p^2}{\omega^2 + i\gamma_D\omega}, \tag{2.1}$$

where $\omega$ is the angular frequency, $\omega_p$ is the plasma frequency of the metal and $\gamma_D$ is the damping rate, which arises from the collisions between the electrons and the lattice ions. For gold, which is the metal of interest in this Work, a typical value for the plasma frequency is $1.4\times10^{16}$ $s^{-1}$ and for the damping rate $4.1\times10^{13}$ $s^{-1}$. Note that optical frequencies are much larger than the damping rate but much smaller than the plasma frequency.

By separating the real and imaginary parts, the dielectric function can be written as

$$\epsilon(\omega) = 1 - \frac{\omega_p^2}{\omega^2 + \gamma_D^2} + i\frac{\omega_p^2\gamma_D}{\omega(\omega^2 + \gamma_D^2)}. \tag{2.2}$$

For high frequencies, meaning short wavelengths like X-rays, the dielectric function approaches unity leading to dielectric behavior and transparence. On the other hand, for low frequencies the real part of $\epsilon$ is negative, which leads to, for example, high reflectivity in the visible and infrared.

Figure 2.1 shows a fit to the Drude model of the measured dielectric constant values[37], both the real and imaginary parts, for gold. Based on the fits, the simple plasma model is valid for wavelengths larger than 700 nm. The real part follows the model fairly well over the whole range, but the model for the imaginary part fails at shorter wavelengths due to the interband transitions of gold.

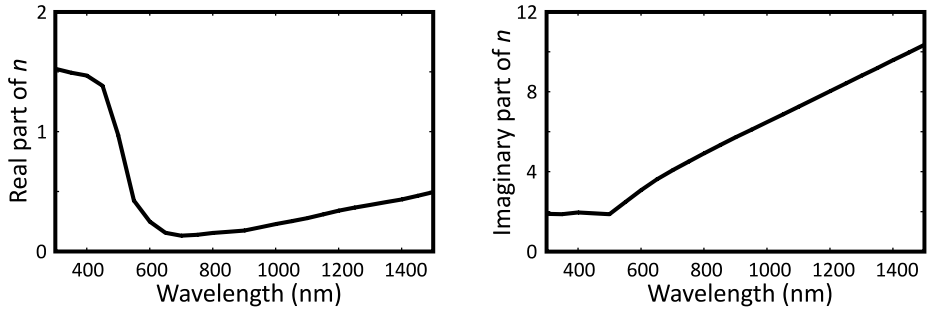


**Figure 2.2** Real and imaginary parts of the index of refraction of gold. Values taken from *Johnson and Christy*[37].

However, we are also interested in the wavelength range below 700 nm, and thus, a better model is required in order to take into account also the interband transions. We use a Drude-Lorentz model written as[36]

$$\epsilon(\omega) = 1 - \frac{\omega_p^2}{\omega^2 + i\gamma_D\omega} + \sum_j \frac{A_j}{\omega_j^2 - \omega^2 - i\gamma_{Dj}\omega}, \tag{2.3}$$

where the summation term represents the contribution of the interband transitions, labeled with letter *j*. Usually it is sufficient to take into account only a few transitions to obtain a good fit to the measured permittivity values.

### Index of refraction

In general, the index of refraction is a complex quantity. The real part of the refractive index is related to the phase of propagation in a medium and the imaginary part leads to absorption. The real and imaginary parts of the index of refraction as a function of wavelength for gold are shown in Figure 2.2. The index of refraction is related to the dielectric function as

$$n(\omega) = \sqrt{\epsilon(\omega)}\,. \tag{2.4}$$

To illustrate the relation between the real and imaginary parts of the dielectric function and the index of refraction, let's consider the dielectric function in the optical regime using the Drude model. For gold in the optical regime, the angular frequency is much higher than the damping rate and the dielectric function can be approximated as

$$\epsilon(\omega) \approx 1 - \frac{\omega_p^2}{\omega^2} + i\frac{\omega_p^2}{\omega^2}\frac{\gamma_D}{\omega}\,. \tag{2.5}$$

Furthermore, the angular frequency is much smaller than the plasma frequency, which leads to the equation

$$\epsilon(\omega) \approx -\left(\frac{\omega_p}{\omega}\right)^2 \left(1 - i\frac{\gamma_D}{\omega}\right). \tag{2.6}$$

The real and imaginary parts of the approximate dielectric function are shown in Figure 2.1 with dashed lines. Clearly the approximation is valid as the dashed lines are barely distinguishable from the solid lines.

The approximate equation for the index of refraction can be obtained using Equation (2.4) and first-order Taylor expansion for the square root, which gives

$$n(\omega) \approx i\frac{\omega_p}{\omega}\sqrt{1 - i\frac{\gamma_D}{\omega}} \approx \frac{1}{2}\frac{\gamma_D}{\omega}\frac{\omega_p}{\omega} + i\frac{\omega_p}{\omega}. \tag{2.7}$$

Thus, the damping rate $\gamma_D$, which leads to the imaginary part of $\epsilon$, is indeed related to the real part of $n$.

Equation (2.6) was obtained by assuming the angular frequency to be smaller than the plasma frequency. In that region the real part of $\epsilon$ is negative. On the other hand, according to Equation (2.7) the real part of $\epsilon$ is related to the imaginary part of $n$. Thus, the negative real part of $\epsilon$ is the dominant factor leading to absorption in metals.

### Skin depth

The electric field at the metal surface always penetrates into the material. The depth of penetration depends on absorption, which is related to the imaginary part of the index of refraction. The complex index of refraction can be written as

$$n(\omega) = n_{Re}(\omega) + in_{Im}(\omega)\,, \tag{2.8}$$

where $n_{Re}(\omega)$ and $n_{Im}(\omega)$ are the real and imaginary parts, respectively. The real and imaginary parts are plotted in Figure 2.2. By plugging Equation (2.8) to the exponential expression for a harmonic plane wave propagating in the *z* direction, the following expression is obtained within the scalar approximation:

$$E(z) = E_0 e^{in(\omega)k_0 z} = E_0 e^{in_{Re}(\omega)k_0 z} e^{-n_{Im}(\omega)k_0 z}\,, \tag{2.9}$$

where $E(z)$ is the electric field, $E_0$ the amplitude of the electric field and $k_0$ is the propagation constant in vacuum ($k_0 = 2\pi/\lambda$). The imaginary part of the refractive index is seen to lead to the attenuation of the field. The attenuation of the intensity as a function of distance *z* is thus

$$I(z) = I_0 e^{-2n_{Im}(\omega)k_0 z} = I_0 e^{-\alpha_{abs} z}\,, \tag{2.10}$$

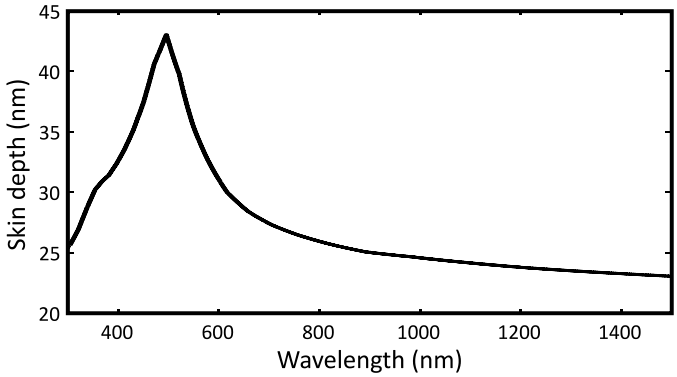


**Figure 2.3** Skin depth as a function of wavelength for gold.

where the last expression is the Beer's law and $\alpha_{abs}$ is the absorption coefficient[38]. The relation between the absorption coefficient and the imaginary part of the refractive index is thus

$$\alpha_{abs} = 2n_{Im}(\omega)k_0 = \frac{2n_{Im}(\omega)\omega}{c}. \tag{2.11}$$

The skin depth is defined as the distance from the surface at which the electric field amplitude has decreased to $1/e$ and the field intensity to $1/e^2$. Thus, the skin depth is related to the imaginary part of the refractive index as[36]

$$\delta = \frac{2}{\alpha_{abs}} = \frac{c}{n_{Im}(\omega)\omega}. \tag{2.12}$$

The skin depth for gold as a function of wavelength is plotted in Figure 2.3 using the values from Johnson and Christy[37]. For wavelengths larger than 500 nm the imaginary part of the refractive index (Figure 2.2) is increasing as a function of wavelength, but the effect is compensated by the $1/\omega$-dependence in Equation (2.12), thus leading to fairly constant skin depth. For the near-infrared wavelengths the skin depth is about 25 nm. In the range between 300 and 500 nm the imaginary part of $n$ is fairly constant, but the skin depth decreases for shorter wavelengths as it is inversely proportional to $\omega$. Therefore, a peak at about 500 nm is observed and the maximum skin depth is 43 nm.

The skin depth is important as the nanostructures investigated in this Work are only 20 nm thick, and thus, the field always extends throughout the particle in the vertical direction. In addition, around 500 nm wavelength in the particles with 50 nm arm width the field at the resonance penetrates through the whole particle also in the transverse direction.

## 2.2. PLASMONS

The optical properties of metals are based on the collective resonant oscillations of the conduction electrons in the structure, called plasmons[36]. There are different types of plasmons based on how they are confined (Figure 2.4). Volume plasmons are not confined and they appear in the bulk metal (Figure 2.4a). They are longitudinal oscillations of the conduction electrons and, thus, cannot be excited with light because of the transverse character of the electric field oscillation of light.

Surface plasmons, also known as surface plasmon polaritons, are confined in one dimension to an interface between two media; a dielectric and a metal (Figure 2.4b). They are oscillations of the conduction electrons near the metal surface, which also leads to an oscillating electric field. Surface plasmons propagate along the interface and the electric field decays in the perpendicular directions, thus confining the energy to the interface.

The permittivities of the materials are essential as the surface plasmons can exist only at interfaces between materials with opposite signs of the real parts of the permittivity. This is fulfilled in the case of a metal and a dielectric material. The permittivity of air or glass is always positive, whereas metals, like gold, have negative real part of the permittivity.

For understanding the properties of surface plasmons, the dispersion relation is important. The dispersion relation of surface plasmons can be derived by starting from the Maxwell's equations and it takes the form[36]

$$k_{SP}(\omega) = k_0(\omega)\sqrt{\frac{\epsilon_1(\omega)\epsilon_2}{\epsilon_1(\omega)+\epsilon_2}}, \tag{2.13}$$

where $k_{SP}(\omega)$ is the propagation constant of the surface plasmon, $k_0(\omega)$ propagation constant of the excitation field, $\epsilon_1(\omega)$ dielectric function of the metal and $\epsilon_2$ dielectric constant of the dielectric material.

Based on Equation (2.13), the surface plasmon propagation constant differs from the propagation constant of the excitation field. Thus, the surface plasmons cannot be excited directly with the incident field, but special phase-matching

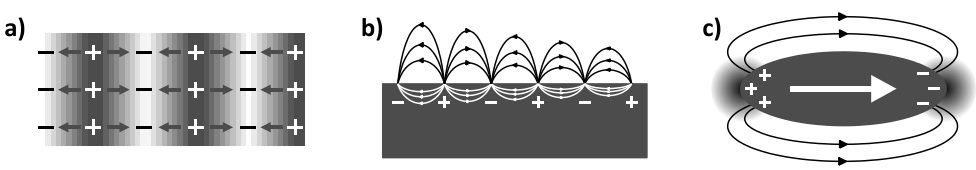


**Figure 2.4** Different types of plasmons. a) Volume plasmon, b) surface plasmon and c) particle plasmon.

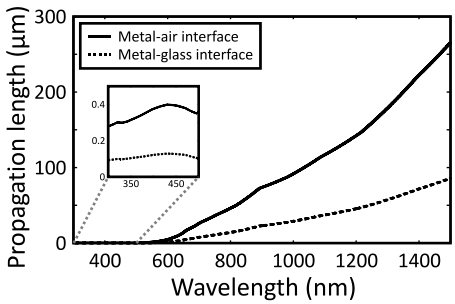


**Figure 2.5** Surface plasmon propagation length. The propation length as a function of wavelength for metal-air and metal-glass interfaces. The plotted graphs correspond to gold as a metal.

techniques, such as prism or grating coupling, are needed to couple light to surface plasmons.

For an ideal conductor the damping rate is zero, and thus also the imaginary part of permittivity $\mathrm{Im}[\epsilon_1(\omega)]$ is zero, which leads to the fact that the surface plasmon propagation constant $k_{SP}$ is always real valued. However, for real metals the dielectric constant $\epsilon_1(\omega)$ is complex, which leads to the imaginary part of $k_{SP}$, which furthermore results in the attenuation of the surface plasmon in the propagation direction. The propagation length is defined as a distance, at which the field intensity has decreased to $1/e$ of the original value, and is

$$L = \frac{1}{2Im[k_{SP}]}. \tag{2.14}$$

The propagation length as a function of wavelength for metal-air and metal-dielectric interfaces is shown in Figure 2.5. At shorter wavelengths the surface plasmons propagate only several hundred nanometers (Figure 2.5 inset). The propagation length increases as a function of wavelength reaching already significant values of several hundred micrometers at the near-infrared. The propagation length depends on the materials on both sides of the interface. For example, for gold the propagation lengths are always larger for the metal-air interface compared to the metal-glass interface.

### Particle plasmons

In metal nanoparticles, the oscillation of the conduction electrons is confined in all three dimensions. Such oscillations are called particle plasmons, or localized surface plasmons. The resonances in metal nanoparticles can be understood by considering the electromagnetic scattering problem for a small conducting particle in an oscillating electromagnetic field.

When the particles are much smaller than the wavelength of light, the quasi-static approximation can be used[36]. It simplifies the problem to a particle in an

electrostatic field. Using the approach for a small spherical particle, it leads to the polarizability $\alpha$ of the particle as[36]

$$\alpha = 4\pi r^3 \frac{\epsilon_1(\omega) - \epsilon_2}{\epsilon_1(\omega) + 2\epsilon_2}, \tag{2.15}$$

where $r$ is the particle radius, $\epsilon_1(\omega)$ the dielectric function of the metal and $\epsilon_2$ the dielectric constant of the surrounding dielectric material. The maximum value of polarizability is obtained when the denominator is minimized. The resonant response also leads to enhanced absorption and scattering. For small or slowly-varying imaginary part of $\epsilon_1$ the condition for the maximum polarizability is

$$Re[\epsilon_1(\omega)] = -2\epsilon_2\,, \tag{2.16}$$

which is called the Fröhlich condition, associated with the particle plasmon resonance of a small metal nanoparticle. The result is valid for particle dimensions below 100 nm[36]. The resonance for polarizability also implies enhancements in the local electromagnetic fields. Note that the resonance enhancement is limited by the imaginary part of the dielectric function of metal.

Thus, by assuming the approximate Drude model for metal (Equation (2.5)), the resonance frequency is obtained from the equation

$$\omega_0 = \frac{\omega_p}{\sqrt{1 + 2\epsilon_2}}. \tag{2.17}$$

For example, the resonance frequency of a small sphere in air is $\omega_p/\sqrt{3} = 0.58\omega_p$ and in a glass ($n = 1.5$) about $0.43\omega_p$. According to the equation the resonance frequency red-shifts as the dielectric constant of the surrounding material is increased.

For particles larger than 100 nm, the quasi-static approximation is not valid, but a rigorous electrodynamic approach is needed. In 1908 Gustav Mie developed a theory describing the scattering and absorption of electromagnetic fields from spherical metal particles. In the approach, the local and scattered fields are expressed as a sum of electric and magnetic multipoles. The approach is valid independent of the particle size, but for small particles the first electric term dominates and has a dipole character, whereas for the larger particles additional terms are needed.

## 2.3. LOCAL FIELD ENHANCEMENT

A characteristic property of metal nanoparticles is the enhancement of the local electromagnetic fields near the surface of the particles. There are two factors, which can enhance the local fields[39]. The plasmon resonances always enhance the local field near the resonance frequency. In addition, tiny features in the particles, such as sharp tips or small gaps, can further enhance the fields.

### Resonance enhancement

At the plasmon resonance, the absorption and scattering cross sections are enhanced, and the local electromagnetic fields in the structure are also enhanced. The local field is enhanced by both the first and the higher-order Mie resonance modes. However, the local field intensities at the higher-order resonances are much lower than the ones related to the fundamental resonances.

For a large resonance enhancement, a narrow width of the resonance is advantageous, as it typically leads to a strong response at the center of the resonance. The strongest local fields are thus usually obtained close to the resonance. However, it has been demonstrated that the strongest local fields do not always exactly match the peak of the resonances[40].

### Lightning rod effect

The lightning-rod effect refers to the strong confinement of the electric fields at sharp tips[41,42]. The effect arises from the localization of the charges in a small volume, which leads to large potential differences, furthermore leading to a very strong local electric field. It is important to note that the lightning rod effect does not depend on the wavelength of the excitation field[43], but it solely depends on the geometry of the structure. The local electromagnetic field can be enhanced also by other small-scale features, such as sharp corners and small gaps[5,44,45].

In addition to the designed features in the samples, the defects arising from the imperfections in the fabrication can also significantly enhance the local fields. The enhancement depends on the spatial location of the defect with respect to the resonance fields. The defects outside the resonance fields attract only very weak local field intensities, whereas the defects overlapping with the resonance field can significantly enhance the local field strength.

## 2.4. NONLINEAR RESPONSE

In common everyday optics, the interaction between light and matter is linear. However, under very strong electric field, which basically means a laser as a light source, the material properties can be modified. Thus, the material response to

the electric field, as characterized by the polarization, is not anymore linear, but nonlinear terms need to be taken into account. The material polarization can be expressed as a power series of the fundamental electric field as[46]

$$\boldsymbol{P}(t) = \chi^{(1)}\boldsymbol{E}(t) + \chi^{(2)}\boldsymbol{E}^2(t) + \chi^{(3)}\boldsymbol{E}^3(t) + \cdots, \tag{2.18}$$

where $\boldsymbol{P}(t)$ is polarization, $\boldsymbol{E}(t)$ electric field, $\chi^{(1)}$ linear susceptibility and $\chi^{(n)}$ the *n*th-order nonlinear susceptibility ($n > 1$). Note that, in general, the fields are vector quantities, and thus, the susceptibilities are tensors.

The higher order terms lead to many interesting phenomena occurring in the material. Without going into details, the possible second-order processes are second-harmonic generation, sum-frequency generation, difference-frequency generation, electro-optic effect and optical parametric oscillation[46]. Similarly, the third-order processes include third-harmonic generation, four-wave mixing and intensity dependent refractive index[46].

### Second-harmonic generation

In second-harmonic generation, a fundamental field at frequency $\omega$ generates an output field at the doubled frequency $2\omega$. Depending on the material, a certain amount of the energy is converted into the frequency-doubled field, and the remaining energy stays in the fundamental field. The process can be understood on the level of photons, where two fundamental photons are needed to produce one frequency-doubled photon (Figure 2.6a). This is simply related to the conservation of the energy.

Another important requirement is the conservation of momentum, which is related to the $\boldsymbol{k}$-vectors. Matching the $\boldsymbol{k}$-vectors of the input and output field is called phase-matching. In this Work, the investigated samples are thin, and thus, the longitudinal phase-matching is not important. Due to the requirement of the transverse phase-matching, two fundamental fields incident on the sample at different angles generate, in addition to the frequency-doubled fields in the original propagation directions, also a second-harmonic field in the direction where the two fields are phase-matched, which is in the middle of the fundamental fields

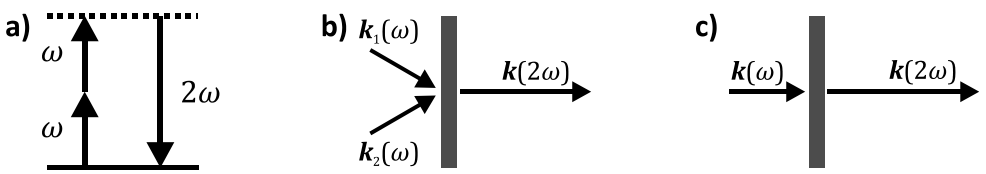


**Figure 2.6** Second-harmonic generation. a) Energy level diagram for second-harmonic generation. b) Conservation of momentum defines the propagation direction of the second-harmonic beam in two-beam experiment and c) one-beam experiment.

(Figure 2.6b). In this Work, the experiments are based on single beams, which leads to parallel fundamental and second-harmonic beams, and the phase-matching condition is always fulfilled (Figure 2.6c).

As discussed before, the plasmon resonances enhance the local electromagnetic field, which interacts with the local surface nonlinearity of the particles leading to enhanced nonlinear response. By considering the plasmon as an oscillator in the Lorentz model, an equation describing the dependence of the second-order nonlinear susceptibility on the resonances can be written as[46]

$$\chi^{(2)} \propto \frac{1}{D^2(\omega)D(2\omega)}, \tag{2.19}$$

where the complex denominator function is

$$D(\omega) = \omega_0^2 - \omega^2 - i2\gamma\omega, \tag{2.20}$$

where $\omega_0$ is the resonance frequency and $\gamma$ is the damping constant, which is actually related to the full width half maximum $\Delta$ of the resonances as

$$\Delta = 2\gamma. \tag{2.21}$$

Note that when this model is taken to the Drude limit ($\omega_0 = 0$), the present and Drude damping rates are related by $\gamma_D = 2\gamma$ (Equation (2.1)). The effect of the resonance at the fundamental frequency is straightforward as stronger and narrower resonance always leads to stronger second-order response. However, the effect of the resonance at the second-harmonic frequency is not trivial. Of course, the resonance can further enhance the second-harmonic response, but at the same time the resonance can also lead to increased attenuation of the generated second-harmonic field in the structure.

### Nonlinear response tensor

In principle, second-harmonic generation is described by the incident light interaction with the material through the second-order susceptibility tensor. However, in nanostructures the second-order susceptibility is a locally varying quantity, and also, the local electromagnetic field at the fundamental frequency is strongly varying in space. Thus, the detailed approach for obtaining the nonlinear response of nanostructures would require accounting for the local field variations, the nonlinear susceptibility tensors, the generated nonlinear sources, and the coupling of the incoming and outgoing fields to the local fields. That approach is very challenging even computationally. Therefore, a simplified approach is used, where the

sample is threat as a “black box”, and only the input and output polarizations are considered[47].

The incoming and outgoing fields are connected by the nonlinear response tensor (NRT) components $A_{jkl}$, which is defined as[47]

$$E_j(2\omega) = \sum_{kl} A_{jkl} E_k(\omega) E_l(\omega) \,, \tag{2.22}$$

where $E_j(2\omega)$ is the outgoing second-harmonic field, and $E_k(\omega)$ and $E_l(\omega)$ are the incoming fundamental fields.

Nonlinear response tensor is a macroscopic parameter, which therefore avoids all the difficulties related to the effects in the nanoscale. The main disadvantage is that the tensor components depend strongly on the experimental setup. However, the approach gives useful information about the macroscopic response of the sample.

In our measurements the sample is always measured at normal incidence, and therefore only the transverse components of the fields are included. In the samples discussed in this Thesis, the coordinate system is fixed based on the symmetry of the sample and the fields are expressed in the same coordinates. The fields are polarized in the (*x*,*y*)-plane and the propagation is in the *z* direction. We typically use a coordinate system, where *y* polarization is chosen to be along the mirror symmetry plane and *x* polarization perpendicular to that. The *j* polarized second-harmonic output field is then obtained from the equation

$$E_j(2\omega) = A_{jxx} E_x^2(\omega) + A_{jyy} E_y^2(\omega) + 2A_{jxy} E_x(\omega) E_y(\omega) \,, \tag{2.23}$$

where *j* is either *x* or *y* and $A_{jkl}$ are the nonlinear response tensor components. Note that the factor of two comes from the fact that for second-harmonic generation the latter two tensor component indices are interchangeable ($A_{jxy}$=$A_{jyx}$).

As second-harmonic generation is an even-order nonlinear optical process, it is very sensitive to the symmetry of the structures[46]. As a common example, the second-harmonic signal in the forward direction from a sphere or a round particle is zero due to the centrosymmetry of the particle. For more complicated particles,

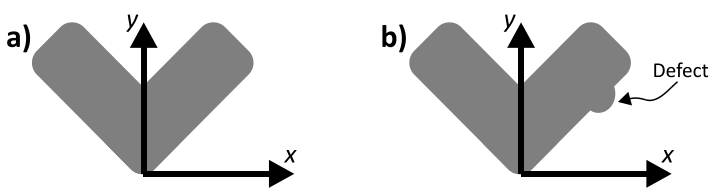


**Figure 2.7** Ideal and broken symmetry. a) An ideal particle with a symmetry plane in *y* direction. b) A particle with symmetry broken by defect.

electric-dipole-type selection rules can be applied in order to figure out the vanishing tensor components. In general, if *y* is the symmetry axis and *x* perpendicular to it (Figure 2.7a), the tensor components with odd number of *x* are forbidden, which can clearly simplify the Equation (2.23).

On the other hand, in the real samples defects in the particles can break the ideal symmetry (Figure 2.7b), which leads to nonzero forbidden components. The symmetry breaking due to the defects is more discussed in the next Section.

### Circular difference response

The structures investigated in this Work ideally have a mirror plane, which means that they are achiral. However, due to imperfections in the fabrication process, the real samples can have small defects or larger deformations, which break the ideal symmetry and make the samples chiral. The chirality can be investigated by comparing the optical responses for left- and right-circular polarizations. In principle, the chirality could be investigated by comparing the response for circular polarizations at the fundamental frequency, but usually the defects are so small that the difference would be marginal. However, second-harmonic generation is extremely sensitive to the symmetry of the particles, and thus, even small-scale defects in the particles can lead to remarkable differences in the second-harmonic responses for the two circular polarizations.

The circular difference response (CDR) at the second-harmonic frequency is defined as the difference between the second-harmonic intensities for the circular polarizations of the fundamental field divided by the average of those two quantities[32]

$$CDR = 2\left|\frac{I_{LCP}(2\omega) - I_{RCP}(2\omega)}{I_{LCP}(2\omega) + I_{RCP}(2\omega)}\right|. \tag{2.24}$$

The sign of the circular difference response value would give information about the handedness of the sample, but as here we were only interested on the level of symmetry breaking the absolute value was taken.

As the chirality is related to the symmetry breaking of the sample, also the ideally forbidden tensor components are not forbidden anymore. It is rather straightforward to show the relation between the circular difference response and the forbidden tensor components. For circular polarizations we know that

$$E_y(\omega) = \pm iE_x(\omega)\,, \tag{2.25}$$

where $\pm$ refers to the different circular polarization states. Furthermore, the *x* and *y* components of the second-harmonic output field can be written as

$$E_x(2\omega) = A_{xxx}E_x^2(\omega) - A_{xyy}E_x^2(\omega) \pm 2iA_{xxy}E_x^2(\omega)\,, \tag{2.26a}$$

$$E_y(2\omega) = A_{yxx}E_x^2(\omega) - A_{yyy}E_x^2(\omega) \pm 2iA_{yxy}E_x^2(\omega)\,. \tag{2.26b}$$

As discussed before, our coordinate system is chosen to have the symmetry plane along the *y* direction. Thus, for ideal samples, the tensor components with odd number of *x* are symmetry forbidden. Therefore, for an ideal sample, the output fields can be written as

$$E_x(2\omega) = \pm 2iA_{xxy}E_x^2(\omega)\,, \tag{2.27a}$$

$$E_y(2\omega) = A_{yxx}E_x^2(\omega) - A_{yyy}E_x^2(\omega)\,. \tag{2.27b}$$

For the *x* polarized output, the first two terms vanish and the phase of the output field indeed depends on the handedness, but the measured intensity does not. For *y* polarized output, the term depending on the handedness of the input polarization vanishes. Therefore, for an ideal sample, with forbidden tensor components equal to zero, the second-harmonic intensity is equal for the left- and right-circular polarizations, leading to zero circular-difference response.

However, if the imperfections in the samples break the ideal symmetry, the values of the forbidden tensor components are increased furthermore leading to difference in the Equation (2.26) for the two circular polarizations. The values of the circular-difference response can be thus used to measure the level of the symmetry breaking in the samples.

## 2.5. DIFFRACTIVE COUPLING

The optical properties of metal nanoparticles based on particle plasmons were discussed in Section 2.2, where the approach implicitly assumed only single particles. However, the extinction cross section of a single particle is very small, and thus, arrays of particles are typically used in experiments. Then, however, the total response of the whole sample may not be a simple sum of the responses of single particles.

The response can be affected by near-field coupling between the particles[13,48-51]. When moving two cylindrical particles closer to each other, clear modifications in the spectra have been observed[13], and similar observations have been obtained also for coupled nanorods[48]. In split-ring resonators, the coupling of the induced magnetic dipoles has been demonstrated to result in the splitting of the resonance peak for the eigenpolarizations[49]. Also two-layer structures of split-ring resonators with varying mutual orientation of the top and bottom particles have been investigated[50].

In more typical cases, however, the basic units are single particles, which are arranged in a square array with a period of several hundred nanometers. The rather large separation between the particles usually makes the near-field coupling relatively unimportant, but the particles can still be coupled through long-range effects.

As discussed before, the plasmon resonances of the particles lead to significant scattering of the electric field. The scattering occurs into all directions, also in the plane of the particles, and thus it is clear that the scattered field from one particle will hit other particles and modify their local fields. Whether this is important or not, depends on the overlap between the plasmon resonances and the array resonances.

### Propagating surface modes and resonance-domain

In the plane of the particles, the scattered fields from different particles interfere with each other. Depending on their relative phase, which depends on the optical distance between the considered particles, the fields may have destructive or constructive interference. A phase difference of $2\pi$ between the scattered fields from two neighboring particles is exactly the same situation as in traditional diffraction by a grating. The only difference is that here the diffractive mode is not coupled out of the grating but it propagates in the plane of the particles, resulting in a type of a surface mode.

Because of the diffractive character of the effect, it can be called diffractive coupling. The grating can couple light into the propagating modes both on the substrate side and on the air side. Structures, where the particles are coupled through the substrate modes and there are no diffraction orders propagating in free space, are called resonance-domain structures.

The diffractive coupling between the particles comes into play at certain wavelengths, which can be derived from matching the tangential components of the wavevectors at the interface as illustrated in Figure 2.8a. Thus we can write

$$k_{mode} = k_t^{inc} + G\,, \tag{2.28}$$

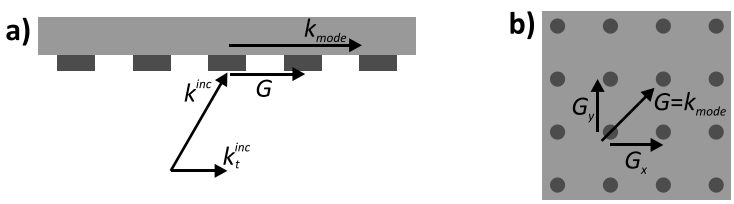


**Figure 2.8** Propagating surface modes. a) Coupling incident light to the grating mode. b) Two-dimensional grating.

where $k_{mode}$ is the propagation constant of the propagating surface mode, $k_t^{inc}$ is the tangential component of the incident wave vector and $G$ is the length of the grating vector. The matching of the $k$-vector components can be also seen as conservation of momentum, when the grating vector contribution to the incident wave is considered as momentum. Our measurements are performed at normal incidence, which leads to zero tangential component of the incident wave.

We have investigated two-dimensional array structures, and therefore, the grating can contribute in both *x* and *y* directions. The absolute value of the total grating vector is thus

$$G = \sqrt{(jG_x)^2 + \left(kG_y\right)^2}, \qquad G_x = G_y = \frac{2\pi}{a}, \tag{2.29}$$

where $G_x, G_y$ are the grating vector components, $j, k$ correspond to different diffraction orders and $a$ is the array period, which is equal in *x* and *y* directions.

The propagating mode wavenumber can be written in terms of wavelength as

$$k_{mode} = n\frac{2\pi}{\lambda}, \tag{2.30}$$

where $n$ is the refractive index of air or substrate and $\lambda$ is the vacuum wavelength. In certain structures the index of refraction can be also an effective parameter defined by the structure. By combining Equations (2.28), (2.29) and (2.30) the equation for the diffraction wavelength can be derived as

$$\lambda_{jk} = n\frac{a}{\sqrt{j^2 + k^2}}. \tag{2.31}$$

Diffractive coupling occurs at clearly different wavelengths on the air and substrate sides. According to Equation (2.31), the higher order diffractive modes are always shifted to shorter wavelengths. Thus, a certain diffractive order on air side can overlap with a higher order diffractive mode on the substrate side, which makes the coupling even more complicated.

### Fano resonances

Usually the resonance of any kind of a simple system has a Lorentzian lineshape, which is a symmetric lineshape. A resonance of a single metal nanoparticle is Lorentzian and, without coupling between the particles, the resonance peak of an array of particles also has Lorentzian shape. On the other hand, real fabricated nanoparticles always have some variation in the dimensions of the particles, which leads to different central wavelengths of the resonances. Such inhomogeneous broadening has a Gaussian profile. The resonance of the whole array is a

sum of the resonances of single particles, which is a convolution of Lorentzian and Gaussian profiles, generally known as the Voigt profile[38]. However, the resonance still has a symmetric lineshape.

In 1961 Ugo Fano discovered a new type of resonance, now named after him as Fano resonance[52]. The main feature is that the resonance is asymmetric. In general, the Fano resonance arises from interference between a narrow resonance and a continuum or a broad resonance[53].

In metal nanostructures Fano resonances can be obtained in different ways. One demonstration is an asymmetric ring/disk cavity structure[54], where the interaction between the ring and disk resonances leads to two resonance modes, one of which is very narrow and the other one very broad. By designing appropriate sample dimensions, the resonances can be tuned to overlap leading to the asymmetric Fano resonance.

In periodic structures of metal nanoparticles the Fano resonances can arise from the interplay between the plasmon resonance, which is a rather broad resonance, and an array resonance, which is basically a discrete resonance[55]. In general, such interplay can lead to for example cutting of the resonance[56-58], a drop in the resonance[55,56] or even bigger changes in the resonance peak. Although the resulting resonance might not always be asymmetric, the resonances are still often called ‘Fano resonances’.

As the Fano resonances arise from coupling effects, they are very sensitive to even small changes in the sample geometry or dielectric environment. This high sensitivity can be very useful in many applications, for example in sensing. Furthermore, the obtained Fano resonances are often very narrow and strong, which can be beneficial in many applications.

# 3.

# METAL NANOSTRUCTURES

Metal nanostructures enable strong confinement of electromagnetic fields and manipulation of light in the nanoscale. These interesting properties show great prospects for future applications. In this Chapter, a review of research on metal nanostructures and their applications is given. Finally, challenges related to the nanostructures' use in nanophotonics applications are discussed.

## 3.1. NANOPARTICLES

Metal nanoparticles have a long historical background in staining of glass windows and ceramics[1]. The colors are due to the absorption of light by small metal nanoparticles embedded in the material. In 1908, Gustav Mie presented a theory explaining the interaction between small spherical particles and electromagnetic field of light[2]. The response of spherical particles and ellipsoids can be calculated analytically[3]. However, for more complicated structures, there is no analytical theory describing their optical properties. Thus, during the past decades many different types of particles and arrangements have been investigated both experimentally and by numerical simulations.

As discussed in Chapter 2.2, the optical properties of metal nanoparticles are based on particle plasmons. The response of the particles is highly dependent on several parameters of the structures, such as dimensions, material, surrounding material and the mutual arrangement of the particles.

In the case of a spherical particle, increasing the size of the particle in the plane of light polarization shifts the resonances towards longer wavelengths. For ellipsoids and rods, the ratio between the long and short axis is important, as the increase in the aspect ratio always shifts the long-axis resonance to longer wavelengths[4,59,60]. The same is typically valid also for more complicated structures, where the long axis then refers to the total length of the structure and the short axis is related to the width of the structures.

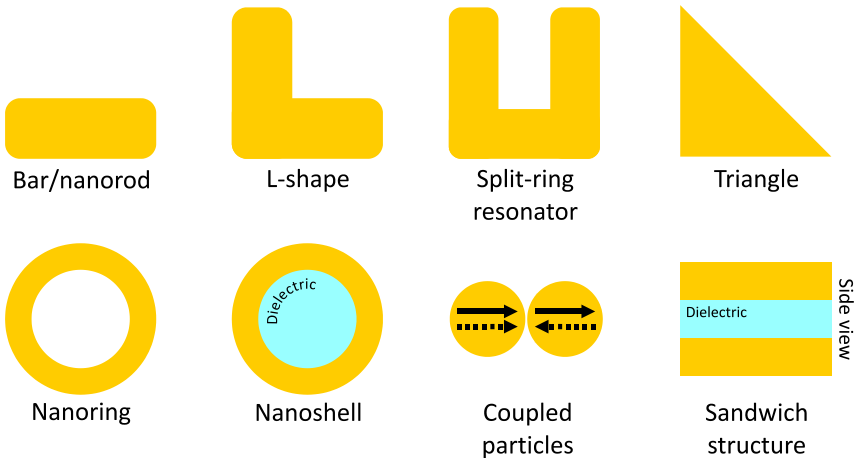


**Figure 3.1** Examples of different types of metal nanoparticles and -structures.

The samples are often investigated as 2D-structures with constant thickness, and thus, the effect of the thickness is usually not considered in analyzing their response. However, when the thickness is comparable to the skin depth of the metal, the fields on top and bottom of the particle are coupled together, which shifts the resonances to longer wavelengths when the thickness decreases[61,62].

The change in the effective refractive index of the surrounding material can simply shift the resonance wavelength[60,63], or it can also more strongly modify the response[64]. The change in the refractive index can be due to having a substrate under the particles instead of air, or the dielectric properties can be modified in a more complicated way for example by burying a particle partly in a dielectric material. The dielectric materials are often described by an effective parameter, which is the average index of refraction of the surrounding materials.

Over the past decades, different types of structures have been investigated (Figure 3.1), like for example bars[65,66], nanowires[67-70], triangles[5,45], nanorings[6], nanoshells[7,8] and split-ring resonators, which are considered more in the next Section. In the past, we have mainly focused on L-shaped particles[30,31], which have been investigated also by others[66,71-73].

Structures with two particles, instead of only single particle, have also been investigated. The coupling between cylindrical particles shifts the resonances, when the particles are moved closer to each other[11-13,74-76]. When the particles are very close to each other or touching each other, the resonances can be even more clearly modified. Another example of coupled structures is the sandwich structures, where a layer of dielectric material separates the particles[77-80]. The coupling has been shown to shift the resonances, but it can also lead to additional resonances due to the coupling.

In general, in a coupled structure, there are actually two types of modes, which can occur[51]. Let's consider, as an example, the modes in the coupled cylindrical particles, shown in Figure 3.1, where the arrows show the direction of the electric field. In one mode, the electric fields at the two particles are in the same phase (solid arrows), and that mode is called a symmetric mode. As it efficiently couples with the excitation field, it is also called a bright mode. The other mode is an antisymmetric mode, where the fields at the two particles oscillate at the opposite phases (dashed arrows). The dipole moment of the antisymmetric mode is zero, and thus it cannot be easily excited, and therefore it is often called a dark mode. However, the excitation of dark modes has been demonstrated theoretically[81,82] and also experimentally[83].

## 3.2. SPLIT-RING RESONATORS

In principle, split-ring resonators are just one type of nanoparticles, but they are investigated so actively that they deserve a more detailed discussion[9,10]. The shape of the split-ring resonator is shown in Figure 3.2. The most interesting properties are based on the resonance in Figure 3.2a, where the electric field oscillation occurs over the whole length of the structure[84]. The oscillation is related to the horizontal polarization of the excitation field.

As the currents in the structure rotate around the center of the structure, it can be understood as a coil having also a strong magnetic field at the center of the structure[49]. Furthermore, the ends of the U-shape have dielectric material in between, which corresponds to a capacitor. Thus, the structure can be considered as an LC-oscillator and the resonance is often called as LC-resonance[85,86]. It can also be called magnetic resonance due to the strong magnetic dipole induced in the structure. Due to the magnetic nature and the nanoscale size, the split-ring resonators are also called nanomagnets[87].

The vertical polarization of the excitation field can be used to excite another resonance, where the field oscillates between the center of the bottom bar and the both ends of the bar (Figure 3.2b)[84]. This resonance is often called plasmonic resonance. It is important to note that the resonance in Figure 3.2a is also plasmonic, but due to its magnetic character different naming is often used.

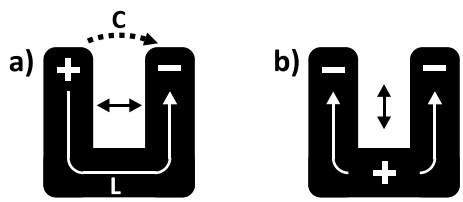


**Figure 3.2** Resonances in split-ring resonators. a) LC-resonance/magnetic resonance. b) Plasmonic resonance.

The resonances in Figure 3.2 are basically related to single particles. However, coupled split-ring resonators can lead to completely new and tunable resonances[50] or the coupling can simply just shift the resonance[88], depending on the mutual arrangement of the units. Also, increasing the thickness of the structures has been observed to shift the resonances to shorter wavelengths[89].

## 3.3. NANOAPERTURES

In addition to nanoparticles on a substrate, also complementary structures with holes, called nanoapertures, in a metal film have been investigated. From elementary considerations, one can expect that the electric field does not pass through an aperture with dimensions smaller than the wavelength of the incoming field[90]. However, sub-wavelength arrays of holes in a metal film can lead to enhanced transmission[90-92]. The transmission peaks can occur at much larger wavelengths than the diameter of the holes and the transmission normalized to the area of the holes can be more than unity. The results were originally explained by surface plasmons induced by the coupling between the incoming light and the periodic structure. Later it has been proposed that the enhanced transmission would result from a waveguide-mode resonance and diffraction[93].

Another interesting aperture structure is complementary split-ring resonator, where the structures are holes in a gold film. Both by numerical simulations and experiments it was found that the resonances in a split-ring resonator for one eigenpolarization actually correspond to the resonances in a complementary structure for the other eigenpolarization[94,95]. Furthermore, the local electric field distributions in a split-ring resonator are similar to the local magnetic field distributions in a complementary structure[94]. This behavior of the structures originates from the Babinet principle[96].

The second-order nonlinear response of aperture structures has been also investigated. The second-harmonic generation has been found to depend on the symmetry and arrangement of the apertures[97], which is similar to the behavior of the nanoparticles. Also second-harmonic generation from complementary split-ring resonators has been measured and the signal levels agreed very well with the traditional structures[95].

## 3.4. METALLIC PHOTONIC CRYSTALS

In general, the term photonic crystal refers to a structure, where the index of refraction varies periodically in the scale of the wavelength[98]. Such structures can be used for guiding light in very small dimensions. Similarly, metallic photonic crystals

refer to materials, where the optical properties of metal nanostructures are modified by the periodicity of the structure. The resonance-domain structures discussed in Section 2.5 can be also considered as metallic photonic crystals as their properties are modified by the periodic structure.

Already in the 90's, arrays of metal spheres in a dielectric support medium and periodic arrays of dots on a silver film have been shown to have a full photonic band gap[99,100] , which means that for certain wavelengths no light is coupled into the structure.

More recent publications have considered periodic arrays of gold nanoparticles or grating lines. The resonance-domain effects have been demonstrated to result in drops in the extinction spectra[56], where the wavelength of the drop depends on the period. The wavelength of the resonance-domain effects depends also on the angle of incidence[101]. By carefully designing the structures, the resonances can be significantly cut from one side leading to very narrow resonances, where the amplitude can be also enhanced[57,58].

## 3.5. METAMATERIALS

Metamaterials are artificial materials with designed properties not found in nature[102]. Some people relate metamaterials only with magnetic resonances and negative index of refraction, but we support a broader definition of designer structures. The optical properties of metamaterials can be artificially tailored by their structural parameters, something which is not possible in naturally occurring materials. This is expected to enable the use of metamaterials in various applications of the future.

The metamaterials often consist of arrays of metal nanoparticles, where the optical properties are typically defined by the properties of the individual particles, but can be furthermore modified by the macroscopic structure and the mutual arrangement of the individual particles.

Metamaterials are often considered as effective media, where conceptually all the individual particles are replaced by a macroscopically homogeneous medium[103]. However, the periodicity of the array structure can couple light into the surface modes, which can remarkably affect the optical response. The coupling depends on the angle of incidence and the effective parameters can be defined also for oblique incidence[104]. For wavelengths much larger than the period, the coupling can be neglected and the effective medium approach is valid. However, for typical metamaterial samples with periods in the range of several 100 nm, the response often depends on the angle of incidence, and thus, it is not fully justified to call them effective materials.

### Negative index of refraction

Metamaterials can be designed for various purposes, but quite often they are associated with the possibility of obtaining negative index of refraction[102,105]. The general condition to obtain negative index of refraction is that the real parts of both the permittivity $\epsilon$ and permeability $\mu$ are negative[106,107]. For metals in the optical regime the real part of the permittivity is negative (Figure 2.1). The effective permeability can be artificially modified by proper design of the structures and negative real part of $\mu$ can be obtained near certain plasmon resonances. For example, by using split-ring resonators, the magnetic resonance (Figure 3.2a) can be utilized to obtain the negative real part of $\mu$, and thus, the negative index of refraction.

The negative index of refraction actually refers to the negative real part of the refractive index. However, for metal structures the imaginary part is also significant, as it is associated with losses. Therefore, for optimizing the structures one needs to consider both the real part and imaginary part of the index of refraction. A figure of merit (FOM) describes the performance of the structure and is defined as[108]

$$FOM = -\frac{n_{Re}}{n_{Im}}, \tag{3.1}$$

where $n_{Re}$ and $n_{Im}$ are the real and imaginary part of the index of refraction, respectively. For optimizing the structures the figure of merit should be as large as possible.

Different kinds of structures with negative index of refraction have been demonstrated. One of the first demonstrations was an array of nanorod pairs, where negative index of refraction was obtained at 1.5 μm[109]. By using a net structure much higher negative refractive index associated with significantly lower losses was achieved[108]. By optimizing the properties of the net structure, negative index of refraction was soon demonstrated also near the visible wavelengths at 780 nm[110]. By using metal-dielectric-metal waveguides, negative index of refraction wavelength was pushed down to 500 nm region[111]. In addition, many papers have been published on obtaining negative index of refraction at microwave frequencies[112-114].

## 3.6. APPLICATIONS

The unique optical properties, easy tailorability and extremely strong local fields in metal nanostructures show great prospects for nanophotonics applications. The

structures have been already utilized in several applications and even more exciting applications are expected to appear in the future.

### Surface-enhanced effects

The strong local fields in metal nanostructures or rough surfaces can be utilized to significantly enhance originally very weak signals. For example, Raman scattering from molecules or second-harmonic generation are typically very weak processes. However, they both depend on higher powers of the local electromagnetic field, and thus, the strong local electric fields can significantly enhance the signals[115].

By using surface-enhanced Raman scattering (SERS), the signal can be enhanced by several orders of magnitude, which enables the detection of even single molecules[14,15]. The enhancement can be obtained by using different methods, like for example, colloidal silver particles in a solution[14], gold-silica nanoshells in a solution[116], periodic arrays of spherical gold nanoparticles near a silver film[117], nanoparticles fabricated to the facet of a fiber[118], or arrays of bridged nanocones[119]. Similarly, second-harmonic generation can be significantly enhanced by the nanoscale roughness of the surfaces[16,17].

### Plasmon sensors

The properties of both surface plasmons and particle plasmons are sensitive to the surrounding material. Thus, even small changes in the surrounding environment can significantly affect the resonances, and enable the plasmons to be used as sensors.

The sensors based on surface plasmons can be realized, for example, by measuring the intensity of the outgoing wave or by examining the angular dependence of the excitation[120]. The increase in the sensitivity by using multiple wavelengths has been also reported[121].

The particle plasmon sensors are based on the fact that the resonance wavelength depends on the surrounding medium[18,19]. Thus, the changes in the dielectric properties of the surrounding material shift the resonance wavelength, and the magnitude of the shift can be further used to estimate the change in the refractive index, and even to estimate the concentration of the added material.

The effect has been used, for example, in nanoscale optical biosensors[122,123], and also real-time optical sensors with very high sensitivity[124]. Closely spaced coupled particles have been demonstrated to increase the sensitivity significantly compared to arrays of single particles[125]. Typically the particles are directly on top of the substrate, but also a different approach based on using a dielectric pillar between the substrate and the particle has been introduced in order to reduce the effect of the substrate[126].

### Negative index of refraction

Several applications for negative index of refraction have been proposed[29]. Metamaterials with negative index of refraction can be utilized to build a perfect lens[28,127], which enables focusing light beyond the diffraction limit. The main feature of a perfect lens is that, in addition to the far field radiation, it focuses also the evanescent waves, which carry the information about the finest details of the object, and which are not recovered by the traditional lenses.

A perfect lens can be used for sub-diffraction optical imaging as demonstrated by using a silver superlens at 365 nm[128]. By using a multilayer structure with alternating layers of positive and negative index of refraction, a magnifying superlens in the visible region, which could be integrated into a far-field microscope, has been demonstrated[129]. Similar to superresolution imaging, a perfect lens can also be used for high-resolution optical lithography.

### Nanoantennas

The concept of nanoantennas has been introduced in general for structures that can be used to control the coupling between the local fields and radiation fields[130]. The coupling can be done by utilizing the plasmon resonances of the structures or by the lightning rod effect, which relies on small features such as sharp tips or nanoscale gaps. The most common approaches are bowtie antennas[131-133] and dipole antennas made of simple nanorods[132].

One application of nanoantennas is in controlling the emission of light from molecules or other emitters[25,26]. Nanoantennas with unidirectional emission pattern have been demonstrated by using a pair of interacting nanorods[134] or a row of nanorods, which acts as an optical Yagi-Uda antenna[135].

### Nanoscale light manipulation

Metal nanostructures can be used in several ways to manipulate the electric field properties and propagation of the field in the nanoscale. Nanofocusing has been demonstrated with a plasmonic lens using radially polarized light[20] and also in a tapered plasmonic structure[21]. A traditional wire grid polarizer is based on parallel conducting wires[136] and also arrays of elliptical nanoholes or nanoparticles can be utilized for polarization dependent transmission[22,137]. Chiral helix structures can be used as circular polarizers[138] and plasmonic polarizers can even be integrated directly on semiconductor lasers[139]. Also miniature wave plates[23] and optical filters[24] can be realized by plasmonic structures.

The propagation of fields on the nanoscale can be controlled by plasmonic waveguides. They can control the propagation of surface plasmons, also around bends, and the field can also be coupled to conventional silicon waveguides[27]. Parallel metal nanowires can guide plasmons in the gap between the wires and

the relative arrangement of the wires can be used to control the properties[69]. Combining surface plasmons in a Y-shaped waveguide has been also demonstrated[140].

By utilizing different ways for controlling the electric fields in the nanoscale one can design full photonic circuits in the nanoscale[141,142]. All the basic circuit elements, like nanoresistors, nanocapacitors and nanoinductors, can be obtained by plasmonic structures[143].

### Other applications

Other possible applications worth mentioning are optical data storage[144], nanolasers based on stimulated emission of surface plasmons[145], applications for biological imaging and biomedicine[59], and the possibility to merge photonics and electronics in the nanoscale[146].

## 3.7. CHALLENGES

Although metal nanostructures have great prospects for future nanophotonics applications, there are still big challenges to overcome. Some of the challenges originate from the fundamental properties of metals. The plasmon resonances, which are the basis of most of the applications, are associated with strong absorption and scattering of the incoming field, which causes significant losses in the structures.

In addition to such fundamental problems there are significant challenges related to the fabrication of the nanostructures. First of all, the smallest obtained linewidth limits the size of the structures, which is essential as rather small structures are needed to have the resonances in the optical regime. There are also differences between various structures. For example, split-ring resonators, which are one of the most common plasmonic structures, tend to have very long overall length, which easily shifts the resonances to the infrared.

The linewidth also limits the array period of the structures, typically to a few hundred nanometers, which can open diffraction orders in the substrate affecting the resonances. Such resonance-domain effects are very often detrimental although they can be also utilized to control the optical response of the structures as demonstrated in *Publications 4* and *5*.

Some of the challenges are related to the imperfections in the fabrication process. Variations in the dimensions of the particles in the sample array lead to inhomogeneous broadening of the resonances peaks. Incorrect fabrication parameters can affect the dimensions of the particles shifting the resonance away from the designed wavelength.

Furthermore, the fabrication process always results in some defects on the surface of the particles. The defects can act as hot spots attracting very strong local electromagnetic fields, which can affect the resonances, but more importantly, they affect the local electromagnetic fields in the structure. The defects are particularly important for second-order nonlinear processes, like second-harmonic generation, where the defects can break the symmetry leading to significant forbidden second-harmonic signals.

Yet another challenge is that the structures usually behave as designed only over very narrow wavelength range, although quite often it would be beneficial to have a broadband operation range.

# 4.

# SAMPLES AND MEASUREMENTS

This Chapter describes the fabrication process and different types of samples investigated in this Work. It also includes a detailed description of the measurement setups for the linear and nonlinear measurements. Also the theory needed for analyzing the measurement data is presented. Finally, numerical methods for simulating the response of the structures are briefly explained.

## 4.1. SAMPLE FABRICATION

### Electron-beam lithography

The samples were fabricated using traditional electron-beam lithography (EBL) illustrated in Figure 4.1[147]. A fused silica substrate was first coated with a layer of electron-beam resist, which is sensitive to the energy of the electron beam. Then, a copper layer was deposited on top of the resist to prevent charging of the sample during electron-beam exposure. Next, the designed structure was written on the resist with electron-beam lithography followed by the development process, which results in the desired pattern in the resist layer. Depending on the type of the resist, the development step removes either the areas exposed to the elec-

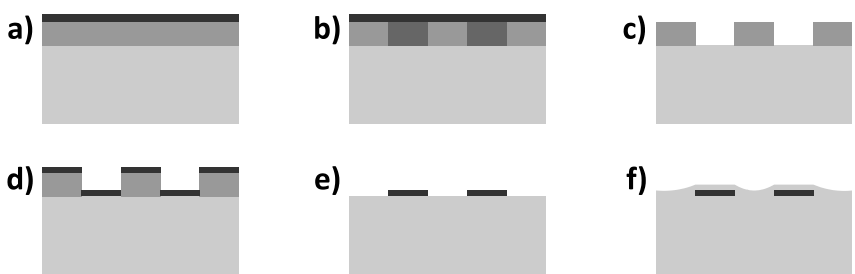


**Figure 4.1** The steps of sample fabrication. a) Deposition of resist and copper layer. b) Electron-beam writing. c) Development. d) Chromium and gold evaporation. e) Lift-off. f) Deposition of protective layer of evaporated quartz.

tron-beam or the areas not exposed. A thin adhesion layer of chromium and the gold were then evaporated on top of the structure. In the lift-off process, the sample is placed into a solvent bath, which dissolves the resist and removes the metal on top of it, resulting in the final gold nanostructures on the substrate. Finally the whole sample was covered with a 20 nm thick layer of evaporated quartz for protection.

Electron-beam lithography enables fabrication of very small metal nanostructures with good quality. The smallest linewidths in our samples have been 50 nm, but fabrication of 10 nm lines has been reported[148]. The writing pattern is defined with a simple black-and-white bitmap, which enables fast modification of the pattern and fabrication of more complex structures. The main disadvantages are the high prices of the fabrication equipment and facilities, and rather slow fabrication speed.

### Sample material – Gold

The most commonly used material for metal nanostructures is gold, which has good plasmonic properties. Silver would be even better as the interband transitions are further away from the typical wavelengths of plasmon resonances. For gold, the interband transitions occur at wavelengths below 620 nm, so already in the visible region, whereas for silver the transitions come into play only below 330 nm. Another advantage is the lower damping rate of silver[149]. However, silver oxidizes quite easily, which can be a problem as the silver oxide layer would modify the dielectric environment of the structure, and thus, also the optical properties of the structures.

Also other options, like different metals, metal alloys, semiconductors and graphene, have been investigated as possible plasmonic materials[149]. Different materials also lead to differences in the quality of the final structures[150]. Each material also has their own challenges in the fabrication, and thus, the fabrication skills are most developed for the most commonly used materials. The quality issues are very important as defects and deformations can significantly affect the optical responses of the structures, especially the nonlinear ones[10,31-33,151-153].

## 4.2. SAMPLES

In this work, T-shaped nanodimers and L-shaped nanoparticles arranged in regular square arrays have been investigated. In addition, samples with modified mutual arrangements of the L particles have been studied.

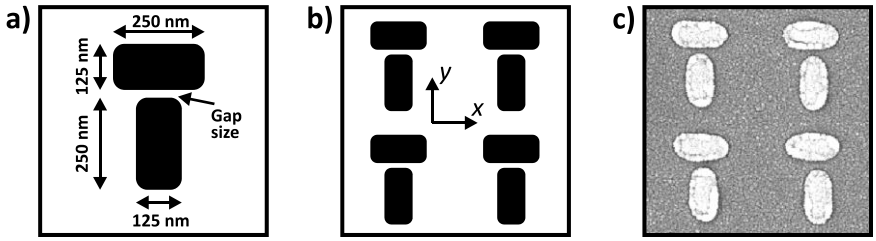


**Figure 4.2** T-shaped nanodimers. a) The geometry of the sample and the dimensions of the horizontal and vertical bars. The gap size is varied between different samples. b) The coordinate system. c) Scanning electron microscope (SEM) image.

## T-nanodimers

Our T-shaped gold nanodimers consist of two bars, a horizontal and a vertical bar, which are both nominally 125 nm wide, 250 nm long and 20 nm thick (Figure 4.2a). The bars are separated by a small gap, which is varied between different sample areas to investigate its effect on the linear and nonlinear optical response of the T-dimers. All the sample areas are 1x1 $mm^2$ and they were fabricated on the same substrate for reliable comparison. The coordinate system, shown in Figure 4.2b, is defined by the eigenpolarizations of the particle along the symmetry axis (*y*) and perpendicular to that (*x*). The particles are arranged in a square array with a period of 500 nm.

## L-nanoparticles

The geometry of the L-shaped gold nanoparticles is shown in Figure 4.3a. The investigated samples have two different arm widths; 50 nm and 100 nm. The arm length between different sample areas is varied from 100 to 300 nm in the 50 nm wide particles and from 150 to 300 nm in the 100 nm wide particles, both in steps of 50 nm. The thickness of the particles is 20 nm. The sample areas are 1x1 $mm^2$ and all the samples were fabricated on a single substrate for reliable comparison.

Similar to the T-shape, the coordinate system is based on the symmetry of the particles with one eigenpolarization along the symmetry axis (*y*) and another one perpendicular to that (*x*) (Figure 4.3b). For the L-particles in *Publication 3* the

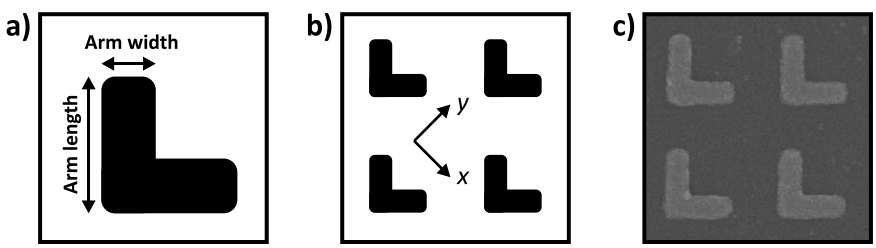


**Figure 4.3** L-shaped nanoparticles. a) The geometry of the L sample. The dimensions are varied between different samples. b) The coordinate system. c) Scanning electron microscope image of a sample array.

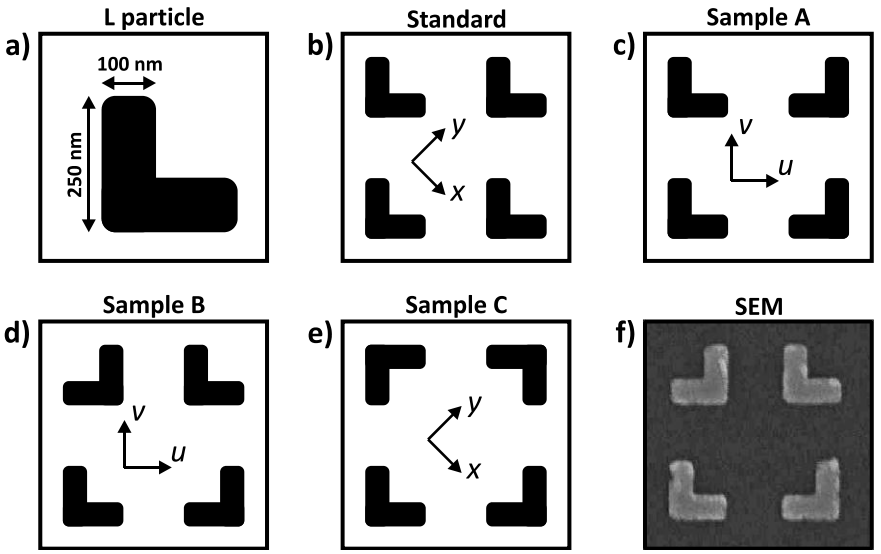


**Figure 4.4** Arrays of L-shaped gold nanoparticles with modified mutual ordering. a) The dimensions of the L particle used as a building block for the arrays. The particle layouts of samples b) Standard array, c) Sample A, d) Sample B, and e) Sample C. f) Scanning electron microscope image of Sample B.

eigenpolarizations are labeled *a* and *b*. The particles are arranged in a square array with a period of 500 nm.

### Resonance-domain metamaterials

The effect of the mutual arrangement of the L particles in a 2-by-2 particle cell was also investigated using sample layouts shown in Figure 4.4. In every sample, the particles are identical L-shaped gold nanoparticles with the arm length of 250 nm, arm width of 100 nm and thickness of 20 nm. The particles are arranged in a square array and the spacing between the particles is 500 nm.

The starting point is the Standard array, where all the particles are oriented the same way (Figure 4.4b), similar to the sample in Figure 4.3b. For Sample A, the particles in every other column are rotated by 90° (Figure 4.4c). The rotation of the particles also changes the symmetry of the whole structure leading to the new eigenpolarizations, *u* and *v*. From Sample A to Sample B the adjacent particles in every other row are pairwise interchanged (Figure 4.4d). This does not change the symmetry of the sample compared to Sample A, and thus, the eigenpolarizations are the same *u* and *v*. Sample C has four-fold symmetry (Figure 4.4e), which should lead to an isotropic optical response. There is no single symmetry plane, and thus, the eigenpolarizations can be more freely chosen. Therefore the same coordinate system as for the Standard array is used.

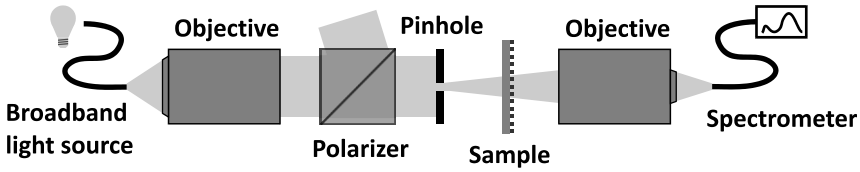


**Figure 4.5** Setup for measuring extinction spectra.

## 4.3. LINEAR MEASUREMENTS

The linear optical properties of the samples were investigated by measuring extinction spectra with a setup shown in Figure 4.5. The extinction spectra include both absorption and scattering, as with the current measurement setup we cannot distinguish those from each other. Both the absorption and scattering contribute to the resonances, but at shorter wavelengths the absorption dominates whereas at longer wavelengths scattering dominates. In the end, however, measuring only a sum of those quantities is not a problem as both contribute to the same resonances.

The measurements were performed at normal incidence using a standard halogen bulb as a broadband light source. The light was coupled to the measurement setup with a multimode optical fiber with a core diameter of 200 µm. The light from the fiber output spreads into a large cone, which was collimated using a microscope objective. As the measured samples were strongly dichroic, controlling the polarization was needed, and it was done with a high quality calcite polarizer.

The sample areas were quite small, in the order of 1 mm x 1 mm, and therefore, a 500 µm diameter pinhole in front of the sample was used to illuminate only the desired sample area. After the pinhole the beam slightly diverges, but can be still assumed to be a plane wave. Using even smaller pinhole would lead to a more diverging beam, which could also affect the measured spectra. After the sample the light was focused with a microscope objective into a fiber connected to a spectrometer. Indeed, two spectrometers, Avantes AvaSpec-2048 for the visible and Avantes NIR256 for the near-infrared, were used to cover a broad spectral range from 400 nm to 1700 nm. The visible-region spectrometer would support also shorter wavelengths down to 323 nm, but the low intensity of the light source over that region leads to poor signal-to-noise ratio, and thus, imprecise results.

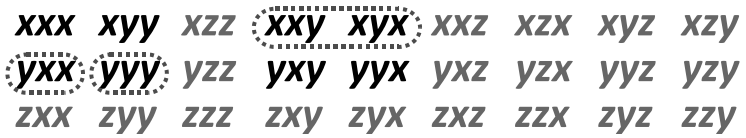


**Figure 4.6** Second-order nonlinear response tensor components. The components including *z* (gray font) are neglected as the measurements are always performed at normal incidence using plane waves. The allowed components are shown with dashed lines.

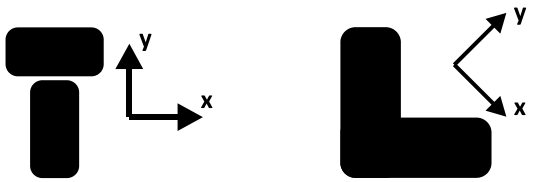


**Figure 4.7** The coordinate systems for T-shaped nanodimers and L-shaped nanoparticles.

## 4.4. NONLINEAR MEASUREMENTS

Several different nonlinear measurements were performed in order to address the nonlinear properties of the samples. All the measurements were based on measuring polarization-dependent second-harmonic generation from the samples, but the details in the polarization control were different.

### Nonlinear response tensor components

The nonlinear response tensor components were discussed in Section 2.4. All the possible input-output combinations are shown in Figure 4.6. All the measurements in this Work are performed at normal incidence, and therefore, all the tensor components including *z* are neglected (grey font color).

Furthermore, as the second-harmonic generation is an even-order nonlinear process, some of the tensor components vanish due to the symmetry of the structures. The coordinate systems for T dimers and L particles are chosen so that the mirror plane of the structure is along *y*-axis for both shapes (Figure 4.7). Thus, their symmetry properties are similar. For ideal samples, the tensor components with odd number of *x* are forbidden[47]. Thus, the only allowed in-plane tensor components are $A_{yxx}$, $A_{yyy}$ and $A_{xxy}=A_{xyx}$ (encircled with dashed lines in Figure 4.6).

### Second-harmonic generation (Publication 1)

The second-harmonic generation measurements were performed using a setup shown in Figure 4.8. The source for the fundamental laser light was an Nd:glass femtosecond laser (wavelength 1060 nm, pulse length 200 fs, repetition rate 82 MHz, average power 300 mW). In *Publication 1*, the second-harmonic signal was

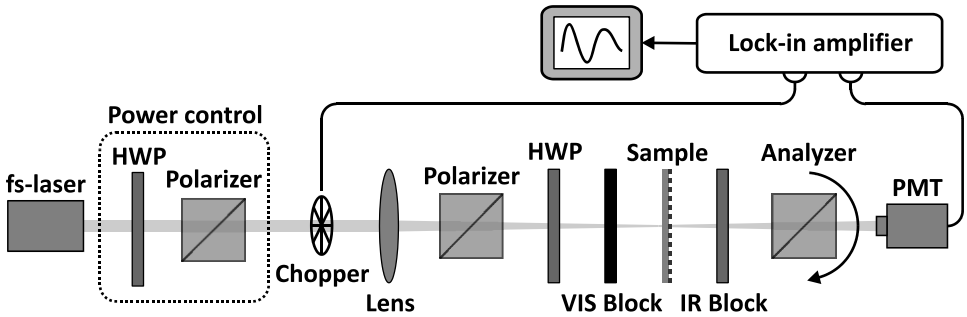


**Figure 4.8** Setup used for measuring second-harmonic generation from T-nanodimers (Publication 1).

measured as a function of the input intensity, which was controlled using a combination of a half-wave plate and a polarizer.

To address the tensorial properties of the samples the measurements were performed for different input-output polarization combinations. The linear input polarization was first cleaned with a high-quality calcite polarizer and then rotated to the desired polarization with a half-wave plate. The measured polarization component of the second-harmonic signal was defined with an analyzer.

To measure only one sample area at a time and also to have sufficiently strong intensity at the sample a focusing lens was used, but with a relatively long focal length to keep the beam close to a plane wave. Note also that the lens was on purpose placed before the polarization control to ensure well defined polarization states. To make sure that the measured second-harmonic signal was coming only from the sample itself, not from the optical components, a visible blocking filter was used before the sample and an infrared blocking filter right after the sample. In addition, a bandpass filter with a center wavelength at the second-harmonic wavelength was used at the input of the detector to minimize the effect of possible background.

For detecting the weak second-harmonic signals, a sensitive photomultiplier tube combined with a lock-in amplifier was used[154]. The fast repetition rate laser was basically considered as a continuous wave laser, which was then modulated with a chopper. By using the lock-in technique, the sensitivity of the measurement system can then be significantly improved.

### Circular difference response (Publication 2)

The chiral symmetry breaking of the samples was measured by circular difference measurements using a setup shown in Figure 4.9, which is very similar to the set-up shown in Figure 4.8. To address the circular polarization states, instead of a half-wave plate, a quarter-wave plate was continuously rotated. Also, an analyzer was not used in these measurements.

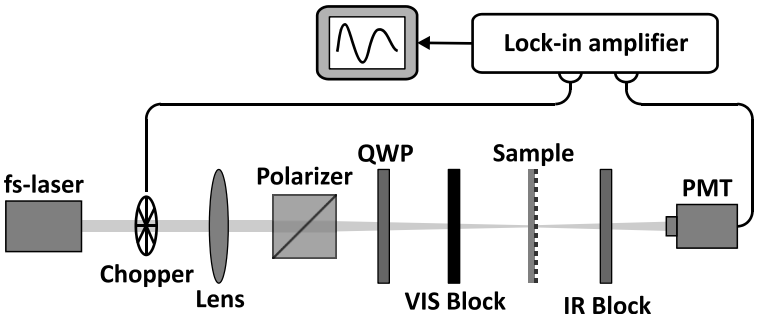


**Figure 4.9** Setup used for circular difference measurements from T-nanodimers (Publication 2).

We also fitted the measurement data to a model based on Equation (2.23), where the electric fields are the fields modulated by the quarter-wave plate and defined as

$$E_x(\omega) = \frac{1}{2}(1-i)\,cos(2\theta)\,E_0(\omega) + \frac{1}{2}(1+i)E_0(\omega)\,, \tag{4.1a}$$

$$E_y(\omega) = \frac{1}{2}(1-i)\,sin(2\theta)\,E_0(\omega)\,, \tag{4.1b}$$

where $\theta$ is the angle of the quarter-wave plate measured from *x* axis. To reduce the effect of the noise on the results, the second-harmonic intensity values for the circular polarization states are taken from the fitted curves.

## Second-harmonic generation (Publication 5)

The second-harmonic generation measurements in *Publication 5* were performed using a setup shown in Figure 4.10, which is very similar to the one used in *Publication 1* and discussed above. Instead of varying the input intensity, a constant intensity was used and a half-wave plate was used to continuously rotate the linear polarization state.

A theoretical model was also fitted to the measured data. The fundamental light from the laser, and after the polarizer, was *x*-polarized and it was rotated

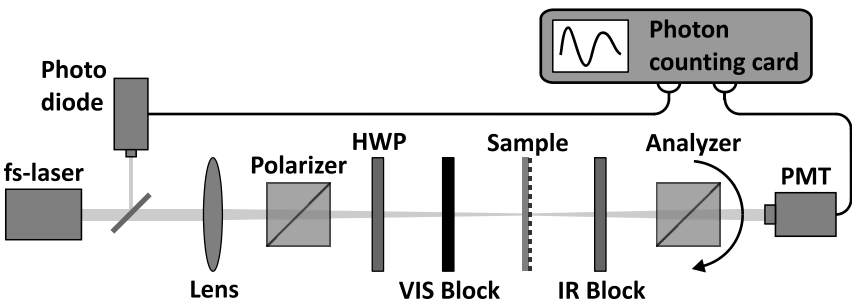


**Figure 4.10** Setup used for measuring second-harmonic generation from L-shaped nanoparticles (Publication 5).

with a half-wave plate. After the half-wave plate, the electric field *x* and *y* components at the fundamental frequency are

$$E_x(\omega) = E_0(\omega)\, cos(2\theta)\ , \qquad E_y(\omega) = E_0(\omega)\, sin(2\theta)\ , \tag{4.2}$$

where $E_0(\omega)$ is the fundamental field amplitude, $\theta$ is the angle between the sample *x* coordinate and the fast axis of the half-wave plate. By using Equation (2.23), the second-harmonic output field as a function of $\theta$ is

$$\begin{aligned} E_j(2\omega) = {} & A_{jxx}E_0^2(\omega)\, cos^2(2\theta) + A_{jyy}E_0^2(\omega)\, sin^2(2\theta) \\ & + A_{jxy}E_0^2(\omega)\, sin(4\theta)\ , \end{aligned} \tag{4.3}$$

which is then used as a fitting model for the measured data. This model is presented here in the (*x*,*y*)-coordinate system, but takes an equal form also in the (*u*,*v*)-system, which is used for some of the samples in *Publication 5*.

Another difference in the setups was the detection system. A sensitive photomultiplier tube was still used as a detector, but now combined with a photon counting card. In principle the system would enable the detection of even single photons, but the presence of the background limits the detection sensitivity. By covering the whole measurement setup with a black cardboard box and using a bandpass filter at the detector input, we have decreased the background to a few photons per second. Thus, already signals with ten photons per second can be easily measured.

## 4.5. ORIENTATIONAL AVERAGE

In *Publications 4* and *5,* we discuss the linear and nonlinear properties of resonance-domain metamaterials, where the mutual orientation between the particles is modified (Figure 4.4). In a simple approach without coupling between the particles, both the linear and nonlinear response of the samples would be orientational averages of the responses of the individual particles.

### Linear response

In the Standard array (Figure 4.4b) the eigenpolarizations are defined by the symmetry of the particles, and thus, one eigenpolarization always couples to only one of the particle resonances. In Samples A and B, the eigenpolarizations *u* and *v* always couple to both *x*- and *y*-polarized resonances of the individual L particles. This should lead to isotropic response, if there is no coupling between the particles. Furthermore, Sample C has four-fold symmetry, which would also imply isotropic response.

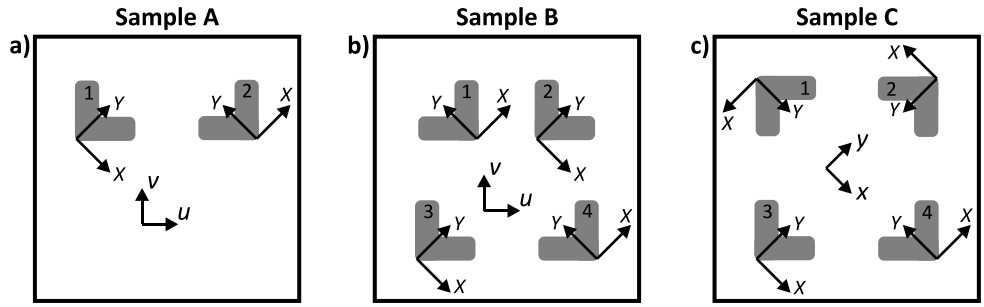


**Figure 4.11** The eigenpolarizations of the samples coupling to the resonances of L particles.

The linear response of the structures is described by the macroscopic response tensor $A_{jk}$, similar to the nonlinear response tensor described in Section 2.4. To predict the response without coupling, let's consider the response tensor of the modified samples, which can be calculated as an orientational average of the tensor components of the individual particles using an equation[155]

$$A_{mn} = \frac{1}{N_p} \sum_{p=1}^{N_p} \sum_{jk} A_{jk}\, cos_p(m,j)\, cos_p(n,k)\,, \tag{4.4}$$

where $A_{mn}$ are the tensor components of the modified sample, $A_{jk}$ are the components of the single particle, $N_p$ is the number of particles in a unit cell and cosine-factors give projections of the particle tensor components into the unit cell coordinates. The summation is performed over all the components $A_{jk}$ and over all the particles in the unit cell. It is important to note that each particle in the unit cell needs to be taken into account as the cosine-factors depend on the orientation of the particle.

As Sample A has only two particles in the unit cell (Figure 4.11a), it is easiest to show the derivation for that. The cosine factors for different combinations are the following:

$$\textbf{\textit{Particle}}\ \mathbf{1}\text{:}\quad cos(u,X) = cos(u,Y) = cos(v,Y) = cos(45°) = \frac{1}{\sqrt{2}}$$
$$cos(v,X) = cos(135°) = -\frac{1}{\sqrt{2}}$$

$$\textbf{\textit{Particle}}\ \mathbf{2}\text{:}\quad cos(u,X) = cos(v,X) = cos(v,Y) = cos(45°) = \frac{1}{\sqrt{2}}$$
$$cos(u,Y) = cos(135°) = -\frac{1}{\sqrt{2}}$$

Note that the sign of the angle does not need to be taken into account as cosine is an even function. The predicted susceptibilities for Sample A can be then derived using Equation (4.4), which gives:

$$\begin{aligned} A_{uu} &= \frac{1}{2}A_{XX} + \frac{1}{2}A_{YY} & A_{uv} &= 0 \\ A_{vu} &= 0 & A_{vv} &= \frac{1}{2}A_{XX} + \frac{1}{2}A_{YY} \end{aligned} \tag{4.5}$$

where the cross-terms $A_{XY}$ and $A_{YX}$ are assumed to be zero as the individual L particle is achiral. The equations for the output fields are written as

$$\begin{aligned} E_u^{out} &= A_{uu}E_u + A_{uv}E_v \,, \\ E_v^{out} &= A_{vu}E_u + A_{vv}E_v \,, \end{aligned} \tag{4.6}$$

where the input polarizations $E_u$ and $E_v$ as a function of the linear input polarization angle are

$$\begin{aligned} E_u &= E_0 \cos\theta \,. \\ E_v &= E_0 \sin\theta \,. \end{aligned} \tag{4.7}$$

By using the results in Equation (4.5), the total output field, simplified by trigonometric identities, can be written as

$$E^{out} = \sqrt{(E_u^{out})^2 + (E_v^{out})^2} = \sqrt{2}A_{uu}E_u \,. \tag{4.8}$$

There is no angle dependence in the output field. Thus, without coupling between the particles, the response would be isotropic.

The only difference between Samples A and B is the ordering of the particles, which does not affect the orientational average. Thus, the result obtained for Sample A is valid also for Sample B.

Although for Sample C the isotropic response is more evident already from the sample layout, a similar approach as for Sample A can also be used to predict the tensor components for Sample C, which gives

$$\begin{aligned} A_{xx} &= \frac{1}{2}A_{XX} + \frac{1}{2}A_{YY} & A_{xy} &= 0 \\ A_{yx} &= 0 & A_{yy} &= \frac{1}{2}A_{XX} + \frac{1}{2}A_{YY} \end{aligned} \tag{4.9}$$

The predicted tensor components are the same as for Sample A, shown in Equation (4.5), although in different coordinates. Thus, by using a similar procedure as

before, it can be shown that the linear response of Sample C is isotropic, as it should be based on the symmetry.

### Second-order nonlinear response

The nonlinear response of the Standard array is defined by the response of the individual particles. If there would be no coupling between the particles, the response of Samples A, B and C would be obtained as orientational averages of the responses of the individual particles. However, as an even-order nonlinear process the second-order response is extremely sensitive to the symmetry of the structures. Therefore, it is important to note, that the Samples A and B now have a symmetry plane along *v* direction, and furthermore, Sample C is centrosymmetric, which should forbid the second-harmonic signal.

To give more insight to the effect of symmetry and to investigate the effect of the coupling between the particles, it is interesting to predict the response of the modified samples based on the orientational average, which is defined using the equation[155]

$$A_{mno}^{(2)} = \frac{1}{N_p} \sum_{p=1}^{N_p} \sum_{jkl} A_{jkl}^{(2)} \, cos_p(m,j) \, cos_p(n,k) \, cos_p(o,l) \, , \tag{4.10}$$

where $A_{jkl}^{(2)}$ are the nonlinear response tensor components for the individual particles, $N_p$ is the number of particles in the unit cell and cosine-factors project the original tensor components to the coordinates of the modified sample.

In the Standard array, the response of the whole sample is defined by the response of the individual particles. Therefore, the nonlinear response tensor components of the Standard array can be used to predict the response of the modified samples. Due to the high quality of the samples, the ideally forbidden tensor components of the Standard array, the ones with odd number of *x*, can be neglected in the summation. Thus, the summation takes into account the components *yyy*, *yxx*, *xxy* and *xyx*. Note that the latter two components need to be taken into account separately as their cosine-factors in the summation might differ although the tensor component values are equal.

The derivation is performed again for Sample A as it has only two particles in the unit cell. The cosine factors are the same as presented earlier. The components with odd number of *u* become zero in the summation as they should due to the symmetry of Sample A. The predicted allowed nonlinear response tensor components are

$$A_{vvv}^{(2)} = \frac{1}{2\sqrt{2}}A_{yyy}^{(2)} + \frac{1}{2\sqrt{2}}A_{yxx}^{(2)} + \frac{1}{2\sqrt{2}}A_{xxy}^{(2)} + \frac{1}{2\sqrt{2}}A_{xyx}^{(2)}, \quad (4.11a)$$

$$A_{vuu}^{(2)} = \frac{1}{2\sqrt{2}}A_{yyy}^{(2)} + \frac{1}{2\sqrt{2}}A_{yxx}^{(2)} - \frac{1}{2\sqrt{2}}A_{xxy}^{(2)} - \frac{1}{2\sqrt{2}}A_{xyx}^{(2)}, \quad (4.11b)$$

$$A_{uuv}^{(2)} = A_{uvu}^{(2)} = \frac{1}{2\sqrt{2}}A_{yyy}^{(2)} - \frac{1}{2\sqrt{2}}A_{yxx}^{(2)} + \frac{1}{2\sqrt{2}}A_{xxy}^{(2)} - \frac{1}{2\sqrt{2}}A_{xyx}^{(2)}. \quad (4.11c)$$

The orientational average of Sample B is equal to Sample A, and thus, the obtained nonlinear response tensor components are the same also for Sample B. For Sample C, the derivation can be done in a similar way resulting in vanishing of all the tensor components.

## 4.6. NUMERICAL METHODS

The work presented in this Thesis is mainly experimental. However, theoretical simulations have also been performed to support and explain the experimental results. For the T-nanodimers, the extinction spectra and the local electric fields were simulated using the Fourier modal method. The code was written in University of Eastern Finland. For L-nanoparticles the simulations were performed using a finite-difference time-domain method with a code written by a colleague in Tampere University of Technology. The numerical simulations were very useful for supporting the experimental observations.

### Fourier modal method (FMM)

The Fourier modal method is also known as rigorous coupled-wave method[156]. It is mostly used for dielectric diffraction gratings but can also be used for metal nanostructures. In the Fourier modal method, the computations are done in the frequency domain. Thus, the permittivity values of the materials measured as a function of wavelength can be conveniently used.

The main points of the method are the discretization of the nanoparticle and expanding the electromagnetic fields into Fourier series. The size of the discretization unit defines the smallest particle details that are taken into account. The number of Fourier components taken into account for the fields defines the smallest possible local field features.

For simulating the spectra, less Fourier components are sufficient, but to be able to precisely simulate the local fields in the structures a rather large number of Fourier terms are needed. On the other hand, increasing the number of terms exponentially increases the calculation time. This is partly the reason why Fourier

modal method is good for simulating the spectra, but is not very well suited for the electric field calculations.

We note that the simulated local fields are not precise enough for quantitative analysis, but can be used in a qualitative way. The results have been qualitatively confirmed by simulations using the finite-difference time-domain method (see next Section).

### Finite-difference time-domain (FDTD)

The finite-difference time-domain method is very commonly used for modeling electromagnetic problems. In the method the structure is discretized, and also, the time-dependent Maxwell's equations are discretized. In the finite-difference time-domain method, as its name suggests, the computations are performed in the time domain. It is very beneficial for calculating the spectra as a short pulse with a broad spectrum can be used as an excitation to calculate a broad spectral range at once. This significantly reduces the time needed for spectral simulations.

However, the spectrally measured permittivity for the material cannot be directly used, but a model needs to be fitted to the measured values, and then, the model function is Fourier transformed into frequency space. The most commonly used model for the gold permittivity is the Drude model, which, however, fails at the shorter wavelengths. Thus, we used a Drude-Lorentz model as explained in Section 2.1, which takes into account the interband transitions leading to a better fit also at shorter wavelengths[157].

# 5.

# RESULTS AND DISCUSSION

This Chapter summarizes the results obtained in the *Publications*. It also includes important results, which were not published in the articles, but are relevant for understanding the whole picture of this Thesis.

## 5.1. T-SHAPED NANODIMERS

Second-harmonic generation from T-shaped gold nanodimers was considered in *Publication 1* and the chirality of the nanodimers in *Publication 2*. This Section describes the basic linear properties of the dimers, demonstrate the locations of the strong local electric fields in the structures and summarize the obtained results from the publications.

### Extinction spectra

The investigated T-shaped nanodimers consist of two similar bars, which have the fundamental resonances related to the short and long axis of the bar (Figure 5.1a). The extinction spectra of an array of bars are shown in Figure 5.1c with dashed lines.

The extinction spectra of an array of T-nanodimers, shown in Figure 5.1c with

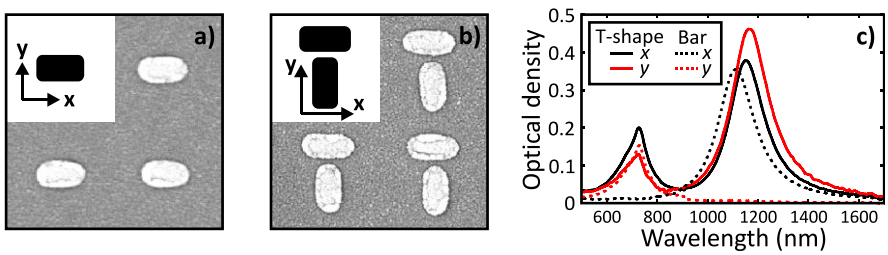


**Figure 5.1** Linear response of T-nanodimers. a) Bar and b) T-shaped nanodimer with the coordinate system and SEM images. c) Comparison of the measured extinction spectra of a T-shaped nanodimer (30 nm gap) and a bar.

solid lines, have two peaks for both eigenpolarizations. The *x* polarization couples to the long axis of the horizontal bar and to the short axis of the vertical bar. Similarly, *y* polarization couples to the short axis of the horizontal bar and to the long axis of the vertical bar. Furthermore, as the bars are located close to each other, the coupling between the bars could modify the resonances. However, based on the measured spectra, the peak locations for the nanodimers are very close to the ones for the bars. The resonances related to the width of the bar are not affected at all. The resonances related to the length of the bar are slightly shifted, but it can be simply due to small differences in the lengths of the bars.

### Local fields

As discussed before, the resonances in the extinction spectra are related to strong local electromagnetic fields in the structure. In the case of a bar, the local electric fields for a polarization along the long axis are located at the ends of the bar.

In T-dimers, the resonance for *x* polarized input field leads to the strong fields at the ends of the horizontal bar (Figure 5.2). However, the fields below the bar are slightly different compared to the fields above, which shows that the gap does affect the local fields, although only slightly for *x* polarization. For *y* polarized input, the local fields are concentrated to the ends of the vertical bar. Now the gap significantly affects the local field as the field in the gap region is much stronger than the field at the bottom end of the bar.

For both polarizations, the local fields are clearly related to the bar resonant with the excitation wavelength for the given polarization. However, the field distributions are not equal to the field distributions of a single bar. First of all, the coupling between the bars can affect the local fields, but the coupling is expected to be relatively weak as the resonance wavelengths corresponding to the length and width of the bar are clearly separated. On the other hand, the gap can nevertheless attract very strong field intensities, which can affect the fields in the whole

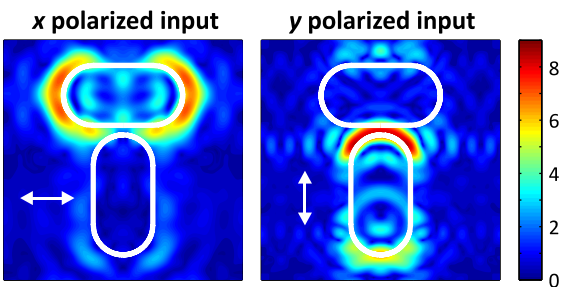


**Figure 5.2** Distributions of the local electric field amplitude at 1060 nm excitation wavelength for a T-nanodimer with 10 nm gap for *x* and *y* input polarizations (shown with white arrows). The local fields are simulated for three-dimensional structures using Fourier modal method (FMM). The color bar shows the local field amplitude scaled to the excitation field.

structure.

Figure 5.2 shows the total electric field amplitude distribution in the structures as it was used for illustrative purpose. However, for analyzing the effect of the local field distribution on the nonlinear response, plotting a certain component of the local field is more useful, as was done in *Publication 1*.

### Second-harmonic generation

In *Publication 1*, we discuss the second-harmonic generation from arrays of T-shaped gold nanodimers. The second-harmonic signal as a function of the gap size was investigated, and the obtained dependence was not trivial at all. In general, small gap sizes lead to stronger second-harmonic response than the larger gap sizes. However, for certain gap sizes the signal almost vanishes, and on the other hand, even rather large gap sizes can lead to surprisingly strong signals.

The results were explained by considering the distributions of the *x*- and *y*-polarized local fields in the structure. We demonstrated that even very small differences in the structure can lead to clear differences in the symmetry of the local field distribution and in the second-harmonic response of the structures. Such subtle differences in the symmetry of the local-field distributions can thus explain the surprising results in the measurements.

### Chirality

In *Publication 2*, we discuss the chirality of the T-nanodimer samples. We investigated the chirality as a function of the gap size by comparing the second-harmonic responses of the structure for left- and right-circularly-polarized light. Although the ideal T-shape is not chiral, in the real samples the vertical bar was slightly tilted with respect to the horizontal bar making the samples chiral. We observed that both the gap size and the tilt of the vertical bar affected the local electric-field distributions.

The measurement results were explained by comparing the local fields for the two circular polarization states. We demonstrated that even small changes in the geometry, and especially in the symmetry of the structures, can significantly affect the local fields, which can be observed as a remarkable circular-difference in the second-harmonic response.

## 5.2. L-SHAPED NANOPARTICLES

The linear properties and local electric fields of L-shaped gold nanoparticles are considered in *Publication 3*. Here we discuss the resonance wavelength depend-

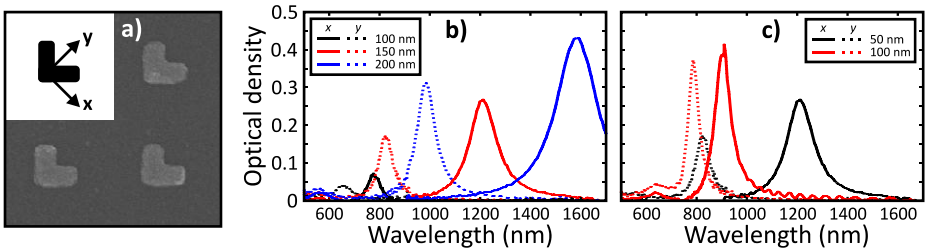


**Figure 5.3** Linear response of L-nanoparticles. a) L-shape, the coordinate system and scanning electron microscope image. Measured extinction spectra for particles with b) different arm lengths (width fixed to 50 nm) and c) different arm widths (length fixed to 150 nm).

ence on the sample dimensions, the characteristics of the local field distributions and briefly summarize the results in the publication.

### Extinction spectra

Due to their anisotropy, the L-shaped gold nanoparticles are strongly dichroic with two fundamental plasmon resonances, one related to the polarization along the mirror axis of the L-shape (*y*) and the other one perpendicular to that (*x*) (Figure 5.3a). The resonance wavelengths depend on the dimensions of the structure. Increasing the length of the arm shifts the resonance to longer wavelengths (Figure 5.3b) and increase in the arm width to shorter wavelengths (Figure 5.3c).

Thus, by changing the dimensions of the L particles the resonances can be easily tuned over very large spectral range, which is important for example for nonlinear optical properties, where the resonance can be tuned to match the wavelength of the fundamental laser light.

### Arm-width-related resonance

In Figure 5.3b, at about 550 nm there are rather broad and weak resonances, which are related to the field oscillation over the width of the arm of the L-shape. The same resonances are observed in Figure 5.3c at a longer wavelength of about 650 nm due to the wider arms of the shape.

In *Publication 3*, we explain the nature and origin of this resonance. Earlier the resonance has been interpreted to be, for example, a volume plasmon, which should not be excitable by light[72]. However, with the support of local field calculations we demonstrated that the resonance is indeed a normal particle plasmon related to the arm width. In fact, at about 500 nm the skin depth of gold is significantly increased (Figure 2.3), which means that the field penetrates deeper into the structure and can therefore be misinterpreted as volume effect.

## Higher-order resonances

The fundamental resonances in Figure 5.3 are the strongest resonances, associated with the strongest local fields, and thus, the ones usually considered. There can be also higher-order resonances, which, however, are usually very weak and can overlap with other short-wavelength resonances, like the arm-width resonance. Nonetheless, the higher-order resonances can provide additional tools for tuning the optical properties of metal nanostructures.

To observe the higher-order resonances there are two important requirements. First of all, a sufficiently large structure is needed to shift the resonances away from the arm-width resonance, and also, to enhance the resonance by the larger volume of the structure. Secondly, good sample quality is required to avoid inhomogeneous broadening of the resonance, which would fade it out.

In *Publication 3*, we have observed four higher-order resonances, two for both eigenpolarizations, for an array of L-shaped nanoparticles with 300 nm arm length and 50 nm arm width. It is more than anyone else has observed for samples with similar dimensions, which is a significant achievement and a proof of very good sample quality. The closest experimental results in terms of the number of observed resonances are the work by Sheridan et al.[158], where they observed three higher-order resonances. However, they investigated crescent shaped structures with a total length of about 1200 nm, which is over twice the total length of our L shapes.

## Local fields

The local fields for an L-shaped nanoparticle at the fundamental resonances are shown in Figure 5.4. The field distribution for *x* polarization is similar to that of a bar with the strong local fields concentrated to the ends of the L-shape. Note, however, that the resonance cannot be considered simply as a resonance of a bent bar as the resonance wavelength does not match the one of a bar with

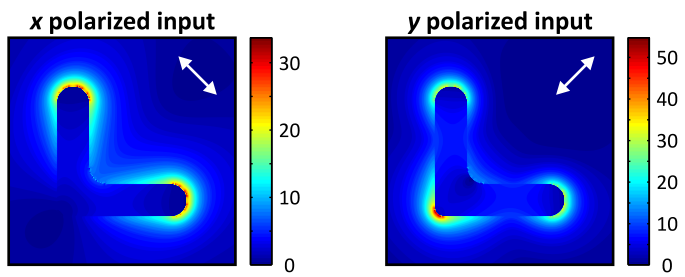


**Figure 5.4** Local electric field distributions at the fundamental resonances for an L particle with 50 nm arm width and 200 nm arm length for *x* and *y* input polarizations. The excitation wavelengths are 1583 nm for *x* polarization and 985 nm for *y* polarization. The local fields are simulated for three-dimensional structures using FDTD. The color bar shows the local field amplitude scaled to the excitation field.

equivalent length.

The field distribution for *y* polarization has three hot spots and the charge oscillations occur along the arms of the structure. We note that such a resonance cannot be excited in a bar since asymmetry is required in the direction of the polarization. In *Publication 3*, the fields at the fundamental resonances as well as the fields at the higher-order resonances and arm-width-related resonances are shown and discussed in more detail.

## 5.3. QUALITY OF THE SAMPLES

Arrays of L-shaped gold nanoparticles have been investigated for quite a long time in our research group. Over the years, the quality of the samples has increased significantly due to better facilities and equipment, and also, development in the fabrication skills. In an old sample from 2004, the L shape is barely recognizable (Figure 5.5a), whereas the new particles with similar dimensions have really good sample quality with almost perfect L shape and even straight parts at the ends of the arms (Figure 5.5b). Even samples with the fairly small linewidth of 50 nm show good quality although they approach the limiting resolution of the current fabrication system (Figure 5.5c).

From the point of view of future applications, good sample quality is essential. In low quality samples, the optical properties are often dominated by the defects, and thus do not match the designed properties. Therefore, with low quality samples, it is practically impossible to optimize the structures for certain functionalities.

### Linear spectra

The effect of the sample quality is already seen in the linear spectra. Table 5.1 shows comparison of the full-width half-maximum (FWHM) values for an old sample[31] and new samples. The new set of samples does not have a sample with exactly the same parameters as the old one. Therefore the resonance wave-

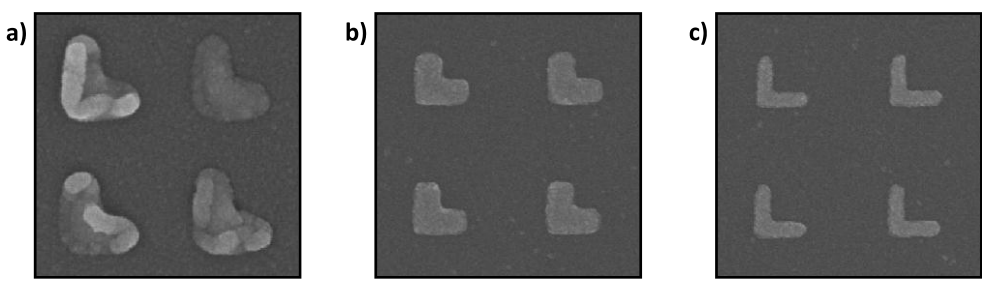


**Figure 5.5** Scanning electron microscope image of a) a sample from 2004, b) a sample with 100 nm arm width from 2009 and c) a sample with 50 nm arm width from 2009.

lengths do not match precisely either, which complicates the comparison as the peak width always decreases with decreasing wavelength. Thus, the table shows two new samples and an estimate of the FWHM linewidth at the old sample resonance wavelength. The estimate is done by simply assuming a linear dependence between the linewidth and the resonance wavelength, which is sufficient for the comparison.

**Table 5.1** Comparison of the widths of the resonances for old and new samples.

| Sample | Arm length | Arm width | Period | Resonance wavelength | FWHM |
|---|---|---|---|---|---|
| **Old**[31] | 190 nm | 110 nm | 400 nm | 1030 nm | ***180 nm*** |
| **New** | 150 nm | 100 nm | 500 nm | 1230 nm | 140 nm |
| **New** | 200 nm | 100 nm | 500 nm | 910 nm | 90 nm |
| **New / Estimate** | - | - | - | 1030 nm | ***110 nm*** |

By comparing the linewidth of the old sample and the respective estimate from the new samples, the effect of the sample quality on the resonance width is clear. The peak of the new sample is approximately 40 % narrower. This is explained by the smaller variation in the sample dimensions leading to less inhomogeneous broadening of the resonance.

## Second-order nonlinear response

As discussed in *Publication 1*, second-harmonic generation is extremely sensitive to the symmetry of the local electric-field distributions. Small defects in the particles can attract very strong spatially confined fields, which can greatly modify the field distributions and affect the second-harmonic generation. In the older samples, it was found that, in some cases, the defects played an important role in the nonlinear response of the structures[33,159]. In the second-harmonic measurements, the ideally forbidden tensor components were always large, and for some samples, even dominant.

**Table 5.2** Comparison of the tensor components for the old and new samples. The values are normalized to the dominant allowed component. The symmetry forbidden components are shown with grey background.

| Sample | *xxx* | *xyy* | *yxx* | *yyy* |
|---|---|---|---|---|
| **Old**[159] | 0.13 | 1.43 | 0.73 | 1 |
| **New**[160] | 0.13 | 0.01 | 1 | 0.04 |
| **New** (***Publication 5***) | 0.05 | 0.09 | 0.41 | 1 |

The comparison of the old and new samples on the level of nonlinear response tensor component values is shown in Table 5.2, where the forbidden components are shown with grey background. In the new samples with significantly increased sample quality, the influence of the defects is greatly suppressed, and the forbid-

den components are always much smaller than the corresponding allowed components[160]. Note, furthermore, that the relative second-harmonic intensities are squares of the values shown in the table, which further suppresses the influence of the forbidden components. This is an essential achievement towards nonlinear metamaterials with truly designable optical properties.

## 5.4. RESONANCE-DOMAIN METAMATERIALS

Resonance-domain metamaterials are arrays of nanoparticles, where the particles are diffractively coupled by propagating surface modes although no diffraction orders propagate in free space. The diffractive coupling greatly affects the linear spectra of the arrays, which are shown and explained in *Publication 4*. The resonance-domain effects arise from the interplay between the plasmon resonance and the grating resonance, and therefore the obtained resonances could also be called Fano resonances (Section 2.5). The diffractive coupling can also be used to control the nonlinear response of the arrays as discussed in *Publication 5*.

### Approach of individual particles

In traditional molecular optics, especially with organic molecules, the intermolecular interactions are typically very weak, and therefore the optical response of a set of molecules can be obtained as the orientational average of the responses of individual molecules. In metal nanostructures, without coupling between the individual particles, the overall response of the sample can be predicted based on a similar approach. The orientational average for the linear and second-order nonlinear response of arrays was discussed in Section 4.5.

### Extinction spectra

The main result in Section 4.5 was that without coupling between the particles the linear optical responses of Samples A, B and C should be equal and also isotropic. Based on the measured spectra, as discussed in *Publication 4*, the simple approach is not valid, but there are significant differences in the spectra of Samples A, B and C.

The results are explained by the diffractive coupling between the particles. The changes in the mutual orientation of the particles double the period in one or two array directions opening diffraction orders, which were designed to occur at the wavelengths of the resonances. Such coupling between the particles significantly affects the linear response of the arrays. In particular, two very similar samples, with the only difference in the ordering of the particles, have completely different spectral responses with either very narrow or ultra-broad resonances.

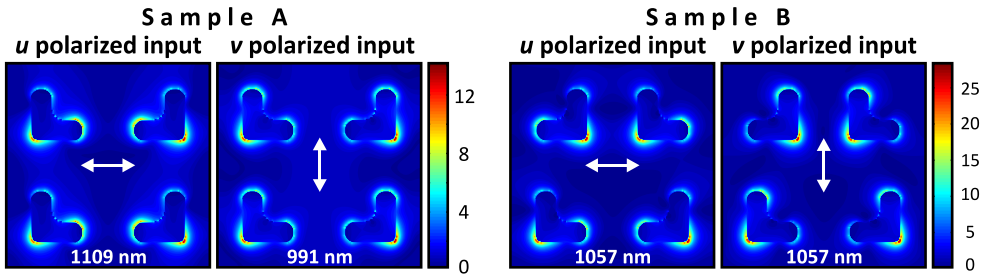


**Figure 5.6** Local electric field distributions in the resonance-domain structures. The local fields at the resonances of Samples A and B for *u* and *v* polarizations. The excitation field polarization is shown with a white arrow and the excitation wavelength at the bottom of the field images. The local fields are simulated for three-dimensional structures using FDTD. The color bar shows the local field amplitude scaled to the excitation field.

## Local fields

The diffractive coupling between the particles arises from the interference between the particle plasmon and the field scattered from the other particles. Thus, in addition to the changes in the spectra, the coupling can affect also the local electric field distributions. As an example, the local fields of Samples A and B for the eigenpolarizations *u* and *v* are shown in Figure 5.6.

The local field amplitudes are related to the resonances in the linear spectra in a straightforward way. The local field maximum for Sample A is about half of the maximum value for Standard array (Figure 5.4), which corresponds to the difference in the resonance amplitudes in the spectra. Similarly, the local field maximum for Sample B is close to the maximum for Standard, which corresponds to almost equal resonance amplitudes.

Furthermore, the coupling can cause even more significant changes in the local fields. The local fields in Figure 5.6 should be compared to the Standard array local field for *y* polarization, shown in Figure 5.4, which is symmetric with respect to the *y* axis due to the symmetry of the particles. In Sample A, the field distributions are clearly modified and are not symmetric within a single particle. However, the fields are symmetric with respect to the unit cell symmetry plane in *v* direction, as should be. Furthermore, the field distributions are clearly different for *u* and *v* polarizations, which is most likely related to the difference of the corresponding plasmonic resonances.

In Sample B, slight asymmetry of the resonances can be also observed. Furthermore, the distributions for the eigenpolarizations are very similar, which correlates with basically equal plasmon resonances.

## Controlling second-harmonic generation

In *Publication 5*, we demonstrate a new concept for tailoring the second-order nonlinear response of arrays of metal nanostructures by controlling the mutual orientation between the particles. The changes in the particle ordering affect the symmetry of the samples, which significantly affects the second-harmonic response. The traditional approach of molecular optics, where overall response of the sample is obtained as the orientational average of the responses of the individual particles, explains the polarization dependence of the response, which arises from the symmetry of the structures.

However, the approach does not take into account the interparticle coupling, which depends on the details of particle ordering and can significantly affect the response. In the Publication, we demonstrate the possibility to either suppress or enhance the second-harmonic response by small changes in the particle ordering. By a minor change in the particle ordering the second-harmonic signal can be enhanced by a factor of up to 50. The differences in the responses are explained in terms of the diffractive coupling between the particles, which is discussed in more detail in *Publication 4*.

# 6.

# CONCLUSIONS AND FUTURE

The plasmon resonances and local electric fields, as well as their effect on the linear and nonlinear response of metal nanostructures, have been investigated. In T-shaped nanodimers, the local electric field distributions play a key role in the second-order nonlinear response of the structures. Even small changes in the particle geometry can significantly affect the nonlinear response.

In L-shaped particles, the improvements in the fabrication process have resulted in very good sample quality, which has several benefits. First of all, multiple higher-order resonances have been experimentally observed, due to the high sample quality. Secondly, the optical properties of the high-quality samples can be precisely designed, as demonstrated by essentially vanishing forbidden second-order tensor components of L-shaped nanoparticles. This is a significant improvement, opening the path towards structures with designable properties and applications.

The possibility for controlling the optical properties in a more precise way has been utilized in the form of resonance-domain structures, where the samples were designed to have strong diffractive coupling between the particles. By tailoring the mutual orientation of the particles, the diffractive coupling, and furthermore the polarization-dependent linear and second-order nonlinear responses, can be controlled in a completely new way.

In earlier works, samples have suffered from the low quality, which has led to broad resonances in the linear response and strong forbidden signals in the second-order nonlinear response. In the low quality nanostructures, defects play an important role in the optical properties, and thus, designing structures with desired optical properties is not straightforward. Especially, designing second-order nonlinear metamaterials has been practically impossible.

In the recent samples, the quality of the nanostructures has finally reached a level, where the imperfections in the structures do not contribute significantly to the optical response. Thus, we are finally at the point, where designing nonlinear

metamaterials is becoming possible. This opens a vast range of possibilities for designing nonlinear materials at the effective medium limit.

An open fundamental question regarding the second-order nonlinear properties of metal nanostructures is whether the response originates from the bulk of the metal or the surface of the structures. That knowledge is important to be able to optimize the locations of the strong local fields for the strongest possible nonlinear response. For example, if the response originates from the surface of the structures, currently only small part of the surface is exploited, which could be solved by proper sample designs.

In the future, the research on resonance-domain metamaterials, which are the first realization of samples with improved quality, will be driven forward. Currently the understanding of the effects is on the qualitative level, but more quantitative understanding would be beneficial for designing structures with optimized properties. That requires both experimental studies of various resonance-domain samples and also deeper understanding of the physics behind the phenomena. As an example of the progress, in recent samples the resonance-domain effects have led to even narrower resonances than the ones observed in *Publication 4*.

In addition to the long-range coupling in resonance-domain structures, near-field coupling can also be utilized for tuning the optical responses. Thus, in addition to the single-particle structures, structures composed of several particles are also particularly interesting. The T-shaped nanodimers investigated in this Work are such structures, but for the current samples the plasmon resonances of the horizontal and vertical bars for a certain polarization occur at very different wavelengths. Thus, the plasmonic coupling between the bars has been relatively weak. In the future, it will be interesting to investigate new dimer, or more generally oligomer, structures, where the plasmon resonance wavelengths of different parts are designed to match, which would lead to stronger interparticle coupling.

All the second-harmonic measurements presented in this Thesis have been performed at a fixed laser wavelength. In the future, it will be interesting to use laser sources tunable over broad spectral range. Tuning the fundamental or harmonic wavelength either close to the resonance or away from the resonance enables more detailed investigation of the effect and importance of the plasmon resonances.

The research on nanoplasmonics, both in our laboratory and in other research groups, is strongly going forwards. A lot of unknown issues have been already addressed, but during the journey plenty of new questions have arisen. To achieve full understanding of the optical properties of metal nanostructures, a lot of work is still needed. Hopefully it will all be worth the effort and one day there will be real everyday applications.

# REFERENCES


[1] S. A. Maier, and H. A. Atwater. *Plasmonics: Localization and guiding of electromagnetic energy in metal/dielectric structures*. Journal of Applied Physics **98**, 011101 (2005).

[2] G. Mie. *Beiträge zur Optik trüber Medien, speziell kolloidaler Metallösungen*. Annalen der Physik **330**, 377-445 (1908).

[3] C. F. Bohren, and D. R. Huffman. *Absorption and Scattering of Light by Small Particles*. John Wiley & Sons (1998).

[4] S. Link, M. B. Mohamed, and M. A. El-Sayed. *Simulation of the Optical Absorption Spectra of Gold Nanorods as a Function of Their Aspect Ratio and the Effect of the Medium Dielectric Constant*. Journal of Physical Chemistry B **103**, 3073 (1999).

[5] J. Kottmann, O. Martin, D. Smith, and S. Schultz. *Spectral response of plasmon resonant nanoparticles with a non-regular shape*. Optics Express **6**, 213-219 (2000).

[6] J. Aizpurua, P. Hanarp, D. S. Sutherland, M. Käll, G. W. Bryant, and F. J. García. *Optical Properties of Gold Nanorings*. Physical Review Letters **90**, 057401 (2003).

[7] S. J. Oldenburg, R. D. Averitt, S. L. Westcott, and N. J. Halas. *Nanoengineering of optical resonances*. Chemical Physics Letters **288**, 243-247 (1998).

[8] R. D. Averitt, S. L. Westcott, and N. J. Halas. *Linear optical properties of gold nanoshells*. J. Opt. Soc. Am. B **16**, 1824-1832 (1999).

[9] C. Rockstuhl, T. Zentgraf, H. Guo, N. Liu, C. Etrich, I. Loa, K. Syassen, J. Kuhl, F. Lederer, and H. Giessen. *Resonances of split-ring resonator metamaterials in the near infrared*. Applied Physics B: Lasers and Optics **84**, 219-227 (2006).

[10] M. W. Klein, C. Enkrich, M. Wegener, and S. Linden. *Second-Harmonic Generation from Magnetic Metamaterials*. Science **313**, 502-504 (2006).

[11] W. Rechberger, A. Hohenau, A. Leitner, J. R. Krenn, B. Lamprecht, and F. R. Aussenegg. *Optical properties of two interacting gold nanoparticles*. Optics Communications **220**, 137-141 (2003).

[12] K. H. Su, Q. H. Wei, X. Zhang, J. J. Mock, D. R. Smith, and S. Schultz. *Interparticle Coupling Effects on Plasmon Resonances of Nanogold Particles*. Nano Letters **3**, 1087-1090 (2003).

[13] T. Atay, J.H. Song, and A. Nurmikko. *Strongly Interacting Plasmon Nanoparticle Pairs: From Dipole-Dipole Interaction to Conductively Coupled Regime*. Nano Letters **4**, 1627-1631 (2004).

[14] K. Kneipp, Y. Wang, H. Kneipp, L. T. Perelman, I. Itzkan, R. R. Dasari, and M. S. Feld. *Single Molecule Detection Using Surface-Enhanced Raman Scattering (SERS)*. Physical Review Letters **78**, 1667-1670 (1997).

[15] K. Kneipp, M. Moskovits, and H. Kneipp. *Surface-enhanced raman scattering: physics and applications*. Springer (2006).

[16] C. K. Chen, A. R.B. de Castro, and Y. R. Shen. *Surface-Enhanced Second-Harmonic Generation*. Physical Review Letters **46**, 145-148 (1981).

[17] M. I. Stockman, D. J. Bergman, C. Anceau, S. Brasselet, and J. Zyss. *Enhanced Second-Harmonic Generation by Metal Surfaces with Nanoscale Roughness: Nanoscale Dephasing, Depolarization, and Correlations*. Physical Review Letters **92**, 057402 (2004).

[18] T. Okamoto, I. Yamaguchi, and T. Kobayashi. *Local plasmon sensor with gold colloid monolayers deposited upon glass substrates*. Optics Letters **25**, 372-374 (2000).

[19] J. J. Mock, D. R. Smith, and S. Schultz. *Local Refractive Index Dependence of Plasmon Resonance Spectra from Individual Nanoparticles*. Nano Letters **3**, 485-491 (2003).

[20] G. M. Lerman, A. Yanai, and U. Levy. *Demonstration of Nanofocusing by the use of Plasmonic Lens Illuminated with Radially Polarized Light*. Nano Letters **9**, 2139-2143 (2009).

[21] M. I. Stockman. *Nanofocusing of Optical Energy in Tapered Plasmonic Waveguides*. Physical Review Letters **93**, 137404 (2004).

[22] R. Gordon, A. G. Brolo, A. McKinnon, A. Rajora, B. Leathem, and K. L. Kavanagh. *Strong Polarization in the Optical Transmission through Elliptical Nanohole Arrays*. Physical Review Letters **92**, 037401 (2004).

[23] A. Drezet, C. Genet, and T. W. Ebbesen. *Miniature Plasmonic Wave Plates*. Physical Review Letters **101**, 043902 (2008).

[24] K. Gurel, B. Kaplan, H. Guner, M. Bayindir, and A. Dana. *Resonant transmission of light through surface plasmon structures*. Applied Physics Letters **94**, 233102 (2009).

[25] J.J. Greffet. *Nanoantennas for Light Emission*. Science **308**, 1561-1563 (2005).

[26] L. Novotny, and N. van Hulst. *Antennas for light*. Nature Photonics **5**, 83-90 (2011).

[27] M. Hochberg, T. Baehr-Jones, C. Walker, and A. Scherer. *Integrated plasmon and dielectric waveguides*. Optics Express **12**, 5481-5486 (2004).

[28] J. B. Pendry. *Negative Refraction Makes a Perfect Lens*. Physical Review Letters **85**, 3966-3969 (2000).

[29] A. Holden. *Towards some real applications for negative materials*. Photonics and Nanostructures - Fundamentals and Applications **3**, 96-99 (2005).

[30] H. Tuovinen, M. Kauranen, K. Jefimovs, P. Vahimaa, T. Vallius, J. Turunen, N. V. Tkachenko, and H. Lemmetyinen. *Linear and Second-Order Nonlinear Optical Properties of Arrays of Noncentrosymmetric Gold Nanoparticles*. Journal of Nonlinear Optical Physics & Materials **11**, 421-432 (2002).

[31] B. Canfield, S. Kujala, K. Jefimovs, J. Turunen, and M. Kauranen. *Linear and nonlinear optical responses influenced by broken symmetry in an array of gold nanoparticles*. Optics Express **12**, 5418-5423 (2004).

[32] B. K. Canfield, S. Kujala, K. Laiho, K. Jefimovs, J. Turunen, and M. Kauranen. *Chirality arising from small defects in gold nanoparticle arrays*. Optics Express **14**, 950-955 (2006).

[33] B. K. Canfield, S. Kujala, K. Jefimovs, T. Vallius, J. Turunen, and M. Kauranen. *Polarization effects in the linear and nonlinear optical responses of gold nanoparticle arrays*. Journal of Optics A: Pure and Applied Optics **7**, S110-S117 (2005).

[34] S. Kujala, B. K. Canfield, M. Kauranen, Y. Svirko, and J. Turunen. *Multipole Interference in the Second-Harmonic Optical Radiation from Gold Nanoparticles*. Physical Review Letters **98**, 167403 (2007).

[35] J. D. Jackson. *Classical electrodynamics*. John Wiley & Sons (1962).

[36] S. Maier. *Plasmonics: Fundamentals and Applications*. Springer (2007).

[37] P. B. Johnson, and R. W. Christy. *Optical Constants of the Noble Metals*. Physical Review B **6**, 4370-4379 (1972).

[38] W. Demtröder. *Laser Spectroscopy*. Springer (2003).

[39] L. Novotny, and B. Hecht. *Principles of Nano-Optics*. Cambridge University Press (2006).

[40] B. M. Ross, and L. P. Lee. *Comparison of near- and far-field measures for plasmon resonance of metallic nanoparticles* . Optics Letters **34**, 896-898 (2009).

[41] A. Hartschuh. *Tip-Enhanced Near-Field Optical Microscopy*. Angewandte Chemie International Edition **47**, 8178-8191 (2008).

[42] J. M. Kontio, H. Husu, J. Simonen, M. J. Huttunen, J. Tommila, M. Pessa, and M. Kauranen. *Nanoimprint fabrication of gold nanocones with ~10 nm tips for enhanced optical interactions*. Optics Letters **34**, 1979-1981 (2009).

[43] M. Schlesinger (editor). *Modern Aspects of Electrochemistry No. 44: Modelling and Numerical Simulations II*. Springer (2009).

[44] K. Li, M. I. Stockman, and D. J. Bergman. *Self-Similar Chain of Metal Nanospheres as an Efficient Nanolens*. Physical Review Letters **91**, 227402 (2003).

[45] A. Sundaramurthy, K. B. Crozier, G. S. Kino, D. P. Fromm, P. J. Schuck, and W. E. Moerner. *Field enhancement and gap-dependent resonance in a system of two opposing tip-to-tip Au*

*nanotriangles*. Physical Review B **72**, 165409 (2005).

[46] R. W. Boyd. *Nonlinear Optics*. Academic Press (2003).

[47] B. K. Canfield, S. Kujala, K. Jefimovs, Y. Svirko, J. Turunen, and M. Kauranen. *A macroscopic formalism to describe the second-order nonlinear optical response of nanostructures*. Journal of Optics A: Pure and Applied Optics **8**, S278–S284 (2006).

[48] J. Aizpurua, G. W. Bryant, L. J. Richter, F. J. García, B. K. Kelley, and T. Mallouk. *Optical properties of coupled metallic nanorods for field-enhanced spectroscopy*. Physical Review B **71**, 235420 (2005).

[49] M. Decker, S. Linden, and M. Wegener. *Coupling effects in low-symmetry planar split-ring resonator arrays*. Optics Letters **34**, 1579-1581 (2009).

[50] N. Liu, H. Liu, S. Zhu, and H. Giessen. *Stereometamaterials*. Nature Photonics **3**, 157-162 (2009).

[51] P. Nordlander, C. Oubre, E. Prodan, K. Li, and M. I. Stockman. *Plasmon Hybridization in Nanoparticle Dimers*. Nano Letters **4**, 899 (2004).

[52] U. Fano. *Effects of Configuration Interaction on Intensities and Phase Shifts*. Physical Review **124**, 1866-1878 (1961).

[53] B. Luk'yanchuk, N. I. Zheludev, S. A. Maier, N. J. Halas, P. Nordlander, H. Giessen, and C. T. Chong. *The Fano resonance in plasmonic nanostructures and metamaterials*. Nature Materials **9**, 707-715 (2010).

[54] F. Hao, P. Nordlander, Y. Sonnefraud, P. V. Dorpe, and S. A. Maier. *Tunability of Subradiant Dipolar and Fano-Type Plasmon Resonances in Metallic Ring/Disk Cavities: Implications for Nanoscale Optical Sensing*. ACS Nano **3**, 643-652 (2009).

[55] A. Christ, Y. Ekinci, H. H. Solak, N. A. Gippius, S. G. Tikhodeev, and O. J. F. Martin. *Controlling the Fano interference in a plasmonic lattice*. Physical Review B **76**, 201405 (2007).

[56] S. Linden, J. Kuhl, and H. Giessen. *Controlling the Interaction between Light and Gold Nanoparticles: Selective Suppression of Extinction*. Physical Review Letters **86**, 4688-4691 (2001).

[57] Y. Chu, E. Schonbrun, T. Yang, and K. B. Crozier. *Experimental observation of narrow surface plasmon resonances in gold nanoparticle arrays*. Applied Physics Letters **93**, 181108 (2008).

[58] B. Auguié, and W. L. Barnes. *Collective Resonances in Gold Nanoparticle Arrays*. Physical Review Letters **101**, 143902 (2008).

[59] P. K. Jain, K. S. Lee, I. H. El-Sayed, and M. A. El-Sayed. *Calculated Absorption and Scattering Properties of Gold Nanoparticles of Different Size, Shape, and Composition: Applications in Biological Imaging and Biomedicine*. Journal of Physical Chemistry B **110**, 7238-7248 (2006).

[60] K. L. Kelly, E. Coronado, L. L. Zhao, and G. C. Schatz. *The Optical Properties of Metal Nanoparticles: The Influence of Size, Shape, and Dielectric Environment*. Journal of Physical Chemistry B **107**, 668-677 (2003).

[61] M. R. Gadsdon, I. R. Hooper, and J. R. Sambles. *Optical resonances on sub-wavelength silver lamellar gratings*. Optics Express **16**, 22003-22028 (2008).

[62] J. Henson, J. DiMaria, and R. Paiella. *Influence of nanoparticle height on plasmonic resonance wavelength and electromagnetic field enhancement in two-dimensional arrays*. Journal of Applied Physics **106**, 093111 (2009).

[63] M. M. Miller, and A. A. Lazarides. *Sensitivity of Metal Nanoparticle Surface Plasmon Resonance to the Dielectric Environment*. Journal of Physical Chemistry B **109**, 21556-21565 (2005).

[64] M. W. Knight, Y. Wu, J. B. Lassiter, P. Nordlander, and N. J. Halas. *Substrates Matter: Influence of an Adjacent Dielectric on an Individual Plasmonic Nanoparticle*. Nano Letters **9**, 2188-2192 (2009).

[65] K.S. Lee, and M. A. El-Sayed. *Dependence of the Enhanced Optical Scattering Efficiency Relative to That of Absorption for Gold Metal Nanorods on Aspect Ratio, Size, End-Cap Shape, and Medium Refractive Index*. Journal of Physical Chemistry B **109**, 20331 (2005).

[66] E. Tatartschuk, E. Shamonina, and L. Solymar. *Plasmonic excitations in metallic nanoparticles: Resonances, dispersion characteristics and near-field patterns*. Optics Express **17**, 8447-8460 (2009).

[67] J. Kottmann, and O. Martin. *Plasmon resonant coupling in metallic nanowires*. Optics Express **8**, 655-663 (2001).

[68] A. Benedetti, M. Centini, C. Sibilia, and M. Bertolotti. *Engineering the second harmonic generation pattern from coupled gold nanowires*. Journal of the Optical Society of America B **27**, 408-416 (2010).

[69] A. Manjavacas, and F. J. Garcia. *Robust Plasmon Waveguides in Strongly Interacting Nanowire Arrays*. Nano Letters **9**, 1285-1289 (2009).

[70] M. A. Schmidt, and P. S. Russell. *Long-range spiralling surface plasmon modes on metallic nanowires*. Optics Express **16**, 13617-13623 (2008).

[71] Y. Jing, Z. Jia-Sen, W. Xiao-Fei, and G. Qi-Huang. *Resonant Modes of L-Shaped Gold Nanoparticles*. Chinese Physics Letters **26**, 067802 (2009).

[72] M. Sukharev, J. Sung, K. G. Spears, and T. Seideman. *Optical properties of metal nanoparticles with no center of inversion symmetry: Observation of volume plasmons*. Physical Review B **76**, 184302 (2007).

[73] J. Sung, E. M. Hicks, R. P. Van Duyne, and K. G. Spears. *Nanoparticle Spectroscopy: Dipole Coupling in Two-Dimensional Arrays of L-Shaped Silver Nanoparticles*. Journal of Physical Chemistry C **111**, 10368-10376 (2007).

[74] P. Olk, J. Renger, M. T. Wenzel, and L. M. Eng. *Distance Dependent Spectral Tuning of Two Coupled Metal Nanoparticles*. Nano Letters **8**, 1174-1178 (2008).

[75] I. Romero, J. Aizpurua, G. W. Bryant, and F. J. García. *Plasmons in nearly touching metallic nanoparticles: singular response in the limit of touching dimers*. Optics Express **14**, 9988-9999 (2006).

[76] J. P. Kottmann, and O. J. F. Martin. *Retardation-induced plasmon resonances in coupled nanoparticles*. Optics Letters **26**, 1096-1098 (2001).

[77] N. Liu, H. Guo, L. Fu, S. Kaiser, H. Schweizer, and H. Giessen. *Plasmon Hybridization in Stacked Cut-Wire Metamaterials*. Advanced Materials **19**, 3628-3632 (2007).

[78] K. H. Su, Q. H. Wei, and X. Zhang. *Tunable and augmented plasmon resonances of Au/SiO2/Au nanodisks*. Applied Physics Letters **88**, 063118 (2006).

[79] A. Dmitriev, T. Pakizeh, M. Käll, and D. S. Sutherland. *Gold-Silica-Gold Nanosandwiches: Tunable Bimodal Plasmonic Resonators*. Small **3**, 294 (2007).

[80] T. Pakizeh, M. S. Abrishamian, N. Granpayeh, A. Dmitriev, and M. Käll. *Magnetic-field enhancement in gold nanosandwiches*. Optics Express **14**, 8240-8246 (2006).

[81] M. Liu, T.W. Lee, S. K. Gray, P. Guyot-Sionnest, and M. Pelton. *Excitation of Dark Plasmons in Metal Nanoparticles by a Localized Emitter*. Physical Review Letters **102**, 107401 (2009).

[82] V. A. Fedotov, M. Rose, S. L. Prosvirnin, N. Papasimakis, and N. I. Zheludev. *Sharp Trapped-Mode Resonances in Planar Metamaterials with a Broken Structural Symmetry*. Physical Review Letters **99**, 147401 (2007).

[83] V. A. Fedotov, N. Papasimakis, E. Plum, A. Bitzer, M. Walther, P. Kuo, D. P. Tsai, and N. I. Zheludev. *Spectral Collapse in Ensembles of Metamolecules*. Physical Review Letters **104**, 223901 (2010).

[84] C. Rockstuhl, F. Lederer, C. Etrich, T. Zentgraf, J. Kuhl, and H. Giessen. *On the reinterpretation of resonances in split-ring-resonators at normal incidence*. Optics Express **14**, 8827-8836 (2006).

[85] T. D. Corrigan, P. W. Kolb, A. B. Sushkov, H. D. Drew, D. C. Schmadel, and R. J. Phaneuf. *Optical plasmonic resonances in split-ring resonator structures: an improved LC model*. Optics Express **16**, 19850-19864 (2008).

[86] S. Linden, C. Enkrich, M. Wegener, J. Zhou, T. Koschny, and C. M. Soukoulis. *Magnetic*

*Response of Metamaterials at 100 Terahertz*. Science **306**, 1351-1353 (2004).

[87] N. Liu, and H. Giessen. *Three-dimensional optical metamaterials as model systems for longitudinal and transverse magnetic coupling*. Optics Express **16**, 21233-21238 (2008).

[88] Y. Zeng, C. Dineen, and J. V. Moloney. *Magnetic dipole moments in single and coupled split-ring resonators*. Physical Review B **81**, 075116 (2010).

[89] H. Guo, N. Liu, L. Fu, H. Schweizer, S. Kaiser, and H. Giessen. *Thickness dependence of the optical properties of split-ring resonator metamaterials*. physica status solidi (b) **244**, 1256-1261 (2007).

[90] T. W. Ebbesen, H. J. Lezec, H. F. Ghaemi, T. Thio, and P. A. Wolff. *Extraordinary optical transmission through sub-wavelength hole arrays*. Nature **391**, 667-669 (1998).

[91] H. F. Ghaemi, T. Thio, D. E. Grupp, T. W. Ebbesen, and H. J. Lezec. *Surface plasmons enhance optical transmission through subwavelength holes*. Physical Review B **58**, 6779-6782 (1998).

[92] D. E. Grupp, H. J. Lezec, T. W. Ebbesen, K. M. Pellerin, and T. Thio. *Crucial role of metal surface in enhanced transmission through subwavelength apertures*. Applied Physics Letters **77**, 1569 (2000).

[93] Q. Cao, and P. Lalanne. *Negative Role of Surface Plasmons in the Transmission of Metallic Gratings with Very Narrow Slits*. Physical Review Letters **88**, 057403 (2002).

[94] T. Zentgraf, T. P. Meyrath, A. Seidel, S. Kaiser, and H. Giessen. *Babinet's principle for optical frequency metamaterials and nanoantennas*. Physical Review B **76**, 033407 (2007).

[95] N. Feth, S. Linden, M. W. Klein, M. Decker, F. B. P. Niesler, Y. Zeng, W. Hoyer, J. Liu, S. W. Koch, J. V. Moloney, and M. Wegener. *Second-harmonic generation from complementary split-ring resonators*. Optics Letters **33**, 1975-1977 (2008).

[96] M. Born, and E. Wolf. *Principles of Optics*. Cambridge University Press (1999).

[97] T. Xu, X. Jiao, G.P. Zhang, and S. Blair. *Second-harmonic emission from sub-wavelength apertures: Effects of aperture symmetry and lattice arrangement*. Optics Express **15**, 13894-13906 (2007).

[98] J. D. Joannopoulos. *Photonic crystals: molding the flow of light*. Princeton University Press (2008).

[99] E. R. Brown, and O. B. McMahon. *Large electromagnetic stop bands in metallodielectric photonic crystals*. Applied Physics Letters **67**, 2138 (1995).

[100] S. C. Kitson, W. L. Barnes, and J. R. Sambles. *Full Photonic Band Gap for Surface Modes in the Visible*. Physical Review Letters **77**, 2670–2673 (1996).

[101] A. Christ, S. G. Tikhodeev, N. A. Gippius, J. Kuhl, and H. Giessen. *Waveguide-Plasmon Polaritons: Strong Coupling of Photonic and Electronic Resonances in a Metallic Photonic Crystal Slab*. Physical Review Letters **91**, 183901 (2003).

[102] V. M. Shalaev. *Optical negative-index metamaterials*. Nature Photonics **1**, 41-48 (2007).

[103] D. R. Smith, D. C. Vier, T. Koschny, and C. M. Soukoulis. *Electromagnetic parameter retrieval from inhomogeneous metamaterials*. Physical Review E **71**, 036617 (2005).

[104] C. Menzel, C. Rockstuhl, T. Paul, F. Lederer, and T. Pertsch. *Retrieving effective parameters for metamaterials at oblique incidence*. Physical Review B **77**, 195328 (2008).

[105] D. R. Smith, J. B. Pendry, and M. C. K. Wiltshire. *Metamaterials and Negative Refractive Index*. Science **305**, 788-792 (2004).

[106] V. G. Veselago. *The electrodynamics of substances with simultaneously negative values of $\varepsilon$ and $\mu$*. Soviet Physics Uspekhi **10**, 509 (1968).

[107] R. A. Depine, and A. Lakhtakia. *A new condition to identify isotropic dielectric-magnetic materials displaying negative phase velocity*. Microwave and Optical Technology Letters **41**, 315-316 (2004).

[108] G. Dolling, C. Enkrich, M. Wegener, C. M. Soukoulis, and S. Linden. *Low-loss negative-index metamaterial at telecommunication wavelengths*. Optics Letters **31**, 1800-1802 (2006).

[109] V. M. Shalaev, W. Cai, U. K. Chettiar, H.K. Yuan, A. K. Sarychev, V. P. Drachev, and A. V. Kildishev. *Negative index of refraction in optical metamaterials*. Optics Letters **30**, 3356-3358 (2005).

[110] G. Dolling, M. Wegener, C. M. Soukoulis, and S. Linden. *Negative-index metamaterial at 780 nm wavelength*. Optics Letters **32**, 53-55 (2007).

[111] H. J. Lezec, J. A. Dionne, and H. A. Atwater. *Negative Refraction at Visible Frequencies*. Science **316**, 430-432 (2007).

[112] A. Sellier, S. N. Burokur, B. Kanté, and A. de Lustrac. *Negative refractive index metamaterials using only metallic cut wires*. Optics Express **17**, 6301-6310 (2009).

[113] B. Wang, J. Zhou, T. Koschny, and C. M. Soukoulis. *Nonplanar chiral metamaterials with negative index*. Applied Physics Letters **94**, 151112 (2009).

[114] S. N. Burokur, A. Sellier, B. Kanté, and A. de Lustrac. *Symmetry breaking in metallic cut wire pairs metamaterials for negative refractive index*. Applied Physics Letters **94**, 201111 (2009).

[115] C. K. Chen, T. F. Heinz, D. Ricard, and Y. R. Shen. *Surface-enhanced second-harmonic generation and Raman scattering*. Physical Review B **27**, 1965-1979 (1983).

[116] S. J. Oldenburg, S. L. Westcott, R. D. Averitt, and N. J. Halas. *Surface enhanced Raman scattering in the near infrared using metal nanoshell substrates*. Journal of Chemical Physics **111**, 4729-4735 (1999).

[117] J. M. Montgomery, A. Imre, U. Welp, V. Vlasko-Vlasov, and S. K. Gray. *SERS enhancements via periodic arrays of gold nanoparticles on silver film structures*. Optics Express **17**, 8669-8675 (2009).

[118] E. J. Smythe, M. D. Dickey, J. Bao, G. M. Whitesides, and F. Capasso. *Optical Antenna Arrays on a Fiber Facet for in Situ Surface-Enhanced Raman Scattering Detection*. Nano Letters **9**, 1132-1138 (2009).

[119] S. Rao, M. J. Huttunen, J. M. Kontio, J. Makitalo, M.R. Viljanen, J. Simonen, M. Kauranen, and D. Petrov. *Tip-enhanced Raman scattering from bridged nanocones*. Optics Express **18**, 23790-23795 (2010).

[120] J. Homola, S. S. Yeea, and G. Gauglitzb. *Surface plasmon resonance sensors: review*. Sensors and Actuators B: Chemical **54**, 3-15 (1999).

[121] K. Johansen, H. Arwin, I. Lundstrom, and B. Liedberg. *Imaging surface plasmon resonance sensor based on multiple wavelengths: Sensitivity considerations*. Review of Scientific Instruments **71**, 3530-3538 (2000).

[122] J. C. Riboh, A. J. Haes, A. D. McFarland, C. R. Yonzon, and R. P. Van Duyne. *A Nanoscale Optical Biosensor: Real-Time Immunoassay in Physiological Buffer Enabled by Improved Nanoparticle Adhesion*. Journal of Physical Chemistry B **107**, 1772-1780 (2003).

[123] G. Raschke, S. Kowarik, T. Franzl, C. Sönnichsen, T. A. Klar, J. Feldmann, A. Nichtl, and K. Kürzinger. *Biomolecular Recognition Based on Single Gold Nanoparticle Light Scattering*. Nano Letters **3**, 935-938 (2003).

[124] A. D. McFarland, and R. P. Van Duyne. *Single Silver Nanoparticles as Real-Time Optical Sensors with Zeptomole Sensitivity*. Nano Letters **3**, 1057-1062 (2003).

[125] S. Enoch, R. Quidant, and G. Badenes. *Optical sensing based on plasmon coupling in nanoparticle arrays*. Optics Express **12**, 3422-3427 (2004).

[126] A. Dmitriev, C. Hägglund, S. Chen, H. Fredriksson, T. Pakizeh, M. Käll, and D. S. Sutherland. *Enhanced Nanoplasmonic Optical Sensors with Reduced Substrate Effect*. Nano Letters **8**, 3893-3898 (2008).

[127] D. R. Smith. *How to Build a Superlens*. Science **308**, 502-503 (2005).

[128] N. Fang, H. Lee, C. Sun, and X. Zhang. *Sub–Diffraction-Limited Optical Imaging with a Silver Superlens*. Science **308**, 534-537 (2005).

[129] I. I. Smolyaninov, Y. J. Hung, and C. C. Davis. *Magnifying Superlens in the Visible Frequency Range*. Science **315**, 1699-1701 (2007).

[130] P. Mühlschlegel, H. J. Eisler, O. J. F. Martin, B. Hecht, and D. W. Pohl. *Resonant Optical Antennas*. Science **308**, 1607-1609 (2005).

[131] D. Fromm, A. Sundaramurthy, P. Schuck, G. Kino, and W. Moerner. *Gap-Dependent Optical Coupling of Single "Bowtie" Nanoantennas Resonant in the Visible*. Nano Letters **4**, 957-961 (2004).

[132] H. Fischer, and O. J. F. Martin. *Engineering the optical response of plasmonic nanoantennas*. Optics Express **16**, 9144-9154 (2008).

[133] P. J. Schuck, D. P. Fromm, A. Sundaramurthy, G. S. Kino, and W. E. Moerner. *Improving the Mismatch between Light and Nanoscale Objects with Gold Bowtie Nanoantennas*. Physical Review Letters **94**, 017402 (2005).

[134] T. Pakizeh, and M. Käll. *Unidirectional Ultracompact Optical Nanoantennas*. Nano Letters **9**, 2343-2349 (2009).

[135] T. H. Taminiau, F. D. Stefani, and N. F. van Hulst. *Enhanced directional excitation and emission of single emitters by a nano-optical Yagi-Uda antenna* . Optics Express **16**, 10858-10866 (2008).

[136] E. Hecht. *Optics*. Addison Wesley (1998).

[137] J. Elliott, I. I. Smolyaninov, N. I. Zheludev, and A. V. Zayats. *Wavelength dependent birefringence of surface plasmon polaritonic crystals*. Physical Review B **70**, 233403 (2004).

[138] M. Thiel, H. Fischer, G. von Freymann, and M. Wegener. *Three-dimensional chiral photonic superlattices*. Optics Letters **35**, 166-168 (2010).

[139] N. Yu, Q. J. Wang, C. Pflügl, L. Diehl, F. Capasso, T. Edamura, S. Furuta, M. Yamanishi, and H. Kan. *Semiconductor lasers with integrated plasmonic polarizers*. Applied Physics Letters **94**, 151101 (2009).

[140] H. Gao, H. Shi, C. Wang, C. Du, X. Luo, Q. Deng, Y. Lv, X. Lin, and H. Yao. *Surface plasmon polariton propagation and combination in Y-shaped metallic channels*. Optics Express **13**, 10795-10800 (2005).

[141] N. Engheta. *Circuits with Light at Nanoscales: Optical Nanocircuits Inspired by Metamaterials*. Science **317**, 1698 (2007).

[142] T. W. Ebbesen, C. Genet, and S. I. Bozhevolnyi. *Surface-plasmon circuitry*. Physics Today **61**, 44 (2008).

[143] N. Engheta, A. Salandrino, and A. Alù. *Circuit Elements at Optical Frequencies: Nanoinductors, Nanocapacitors, and Nanoresistors*. Physical Review Letters **95**, 095504 (2005).

[144] H. Ditlbacher, B. Lamprecht, A. Leitner, and F. R. Aussenegg. *Spectrally coded optical data storage by metal nanoparticles*. Optics Letters **25**, 563-565 (2000).

[145] M. A. Noginov, G. Zhu, A. M. Belgrave, R. Bakker, V. M. Shalaev, E. E. Narimanov, S. Stout, E. Herz, T. Suteewong, and U. Wiesner. *Demonstration of a spaser-based nanolaser*. Nature **460**, 1110-1112 (2009).

[146] E. Ozbay. *Plasmonics: Merging Photonics and Electronics at Nanoscale Dimensions*. Science **311**, 189-193 (2006).

[147] C. Vieu, F. Carcenac, A. Pepin, Y. Chen, M. Mejias, A. Lebib, L. Manin-Ferlazzo, L. Couraud, and H. Launois. *Electron beam lithography: resolution limits and applications*. Applied Surface Science **164**, 111-117 (2000).

[148] A. Grigorescu, M. C. van der Krogt, C. Hagen, and P. Kruit. *10 nm lines and spaces written in HSQ, using electron beam lithography*. Microelectronic Engineering **84**, 822-824 (2007).

[149] P. West, S. Ishii, G. Naik, N. Emani, V. Shalaev, and A. Boltasseva. *Searching for better plasmonic materials*. Laser & Photonics Reviews **4**, 795-808 (2010).

[150] J. M. Kontio, J. Simonen, J. Tommila, and M. Pessa. *Arrays of metallic nanocones fabricated by UV-nanoimprint lithography*. Microelectronic Engineering **87**, 1711-1715 (2010).

[151] B. K. Canfield, H. Husu, J. Kontio, J. Viheriälä, T. Rytkönen, T. Niemi, E. Chandler, A. Hrin, J. A. Squier, and M. Kauranen. *Inhomogeneities in the nonlinear tensorial responses of arrays of*

*gold nanodots*. New Journal of Physics **10**, 013001 (2008).

[152] J. A. H. van Nieuwstadt, M. Sandtke, R. H. Harmsen, F. B. Segerink, J. C. Prangsma, S. Enoch, and L. Kuipers. *Strong Modification of the Nonlinear Optical Response of Metallic Subwavelength Hole Arrays*. Physical Review Letters **97**, 146102 (2006).

[153] M. D. McMahon, R. Lopez, R. F. Haglund Jr., E. A. Ray, and P. Bunton. *Second-harmonic generation from arrays of symmetric gold nanoparticles*. Physical Review B **73**, 041401 (2006).

[154] W. J. Witteman. *Detection and Signal Processing: Technical Realization*. Springer (2006).

[155] P. N. Prasad, and D. J. Williams. *Introduction to nonlinear optical effects in molecules and polymers*. John Wiley & Sons (1991).

[156] O. K. Ersoy. *Diffraction, Fourier Optics and Imaging*. John Wiley and Sons (2007).

[157] A. Vial, A. S. Grimault, D. Macías, D. Barchiesi, and M. L. de la Chapelle. *Improved analytical fit of gold dispersion: Application to the modeling of extinction spectra with a finite-difference time-domain method*. Physical Review B **71**, 085416 (2005).

[158] A. K. Sheridan, A. W. Clark, A. Glidle, J. M. Cooper, and D. R. S. Cumming. *Multiple plasmon resonances from gold nanostructures*. Applied Physics Letters **90**, 143105 (2007).

[159] S. Kujala, B. K. Canfield, M. Kauranen, Y. Svirko, and J. Turunen. *Multipolar analysis of second-harmonic radiation from gold nanoparticles*. Optics Express **16**, 17196-17208 (2008).

[160] H. Husu, K. Koskinen, J. Laukkanen, M. Kuittinen, and M. Kauranen. *Sample Quality and Second-Harmonic Generation from Gold Nanoparticles*. Nonlinear Optics, Quantum Optics, accepted for publication.

## Publication 1

Brian K. Canfield, Hannu Husu, Janne Laukkanen, Benfeng Bai,
Markku Kuittinen, Jari Turunen, and Martti Kauranen

# *Local Field Asymmetry Drives Second-Harmonic Generation in Noncentrosymmetric Nanodimers*

Nano Letters **7**, 1251 (2007)

## Publication 2

Hannu Husu, Brian K. Canfield, Janne Laukkanen,
Benfeng Bai, Markku Kuittinen, Jari Turunen, Martti Kauranen

***Chiral Coupling in Gold Nanodimers***

Applied Physics Letters **93**, 183115 (2008)

## Publication 3

Hannu Husu, Jouni Mäkitalo, Janne Laukkanen, Markku Kuittinen, Martti Kauranen

***Particle plasmon resonances in L-shaped gold nanoparticles***

Optics Express **18**, 16601 (2010)

## Publication 4

Hannu Husu, Jouni Mäkitalo, Roope Siikanen, Goëry Genty, Henna Pietarinen, Joonas Lehtolahti, Janne Laukkanen, Markku Kuittinen, Martti Kauranen

***Spectral control in anisotropic resonance-domain metamaterials***

Optics Letters **36**, 2375 (2011)

## Publication 5

Hannu Husu, Roope Siikanen, Joonas Lehtolahti, Janne Laukkanen,
Markku Kuittinen, Martti Kauranen

***Metamaterials with tailored nonlinear optical response***

Submitted to Nano Letters

Tampereen teknillinen yliopisto
PL 527
33101 Tampere

Tampere University of Technology
P.O.B. 527
FI-33101 Tampere, Finland

ISBN 978-952-15-2690-9
ISSN 1459-2045